


 Cite this: *Lab Chip*, 2021, 21, 254

## Engineering inclined orientations of piezoelectric films for integrated acoustofluidics and lab-on-a-chip operated in liquid environments

 Yong-Qing Fu, <sup>\*a</sup> Hua-Feng Pang, <sup>ab</sup> Hamdi Torun, <sup>a</sup> Ran Tao, <sup>ac</sup> Glen McHale, <sup>d</sup> Julien Reboud, <sup>e</sup> Kai Tao, <sup>f</sup> Jian Zhou, <sup>g</sup> Jingting Luo, <sup>c</sup> Desmond Gibson, <sup>h</sup> Jikui Luo <sup>i</sup> and PingAn Hu <sup>j</sup>

Different acoustic wave modes are required for effective implementation of biosensing and liquid actuation functions in an acoustic wave-based lab-on-a-chip. For efficient sensing in liquids, shear waves (either a thickness-shear bulk wave or a shear-horizontal surface acoustic wave) can achieve a high sensitivity, without significant loss of acoustic wave energy. On the other hand, longitudinal bulk waves or out-of-plane displacement waves (such as Rayleigh waves) enable efficient sampling functions and liquid manipulation. However, there are significant challenges in developing a lab-on-a-chip to efficiently generate multiple wave modes and perform both these functions on a single piezoelectric substrate, especially when a single crystalline orientation is available. This paper highlights the latest progress in the theories and techniques to deliver both sensing and microfluidic manipulation functions using engineered inclined-angled piezoelectric films, allowing for the simultaneous generation of longitudinal (or Rayleigh) and thickness-shear bulk (or shear-horizontal surface acoustic) waves. Challenges and theoretical constraints for generating various wave modes in the inclined films and techniques to efficiently produce inclined columnar and inclined crystalline piezoelectric films using sputtering deposition methods are presented. Applications of different wave modes in the inclined film-based lab-on-chips with multiple sensing and acoustofluidic functions are also discussed.

 Received 3rd September 2020,  
 Accepted 20th November 2020

DOI: 10.1039/d0lc00887g

[rsc.li/loc](http://rsc.li/loc)

## 1. Introduction

Piezoelectric materials have the unique property of generating electricity when they are subjected to external deformation/

pressure; and *vice versa*, they are able to perform actuation functions through geometrical changes when external electrical fields are applied. These materials include:<sup>1</sup> (1) bulk crystals of quartz (SiO<sub>2</sub>), lithium tantalite (LiTaO<sub>3</sub>), lithium niobate (LiNbO<sub>3</sub>), sapphire (Al<sub>2</sub>O<sub>3</sub>), lead zirconate titanate (Pb(Zr,Ti)O<sub>3</sub>, PZT), barium strontium titanate (BaSrTiO<sub>3</sub>), *etc.*; (2) piezoelectric thin films such as PZT, zinc oxide (ZnO), aluminium nitride (AlN), LiNbO<sub>3</sub>, gallium nitride (GaN), and boron nitride (BN); and (3) piezo-polymers such as polyvinylidene fluoride (PVDF), polymer-ceramic composites, *etc.* By depositing metal electrodes on the top and bottom surfaces of a piezoelectric material, a bulk acoustic wave (BAW), in either a longitudinal mode or a thickness-shear mode (TSM), can be generated when electrical signals are applied to these two electrodes as illustrated in Fig. 1a and b. A common example is a quartz crystal microbalance (QCM), with a TSM wave mode generated in a quartz crystal sandwiched between two electrodes, which have been commercially used in various sensing applications. Film bulk acoustic resonators (FBARs, with a piezoelectric film on top of a membrane structure) and solidly mounted resonators (SMRs, with a piezoelectric film on stacks of alternate layers of low and high acoustic impedance forming a Bragg acoustic reflector) have

<sup>a</sup> Faculty of Engineering and Environment, Northumbria University, Newcastle upon Tyne, NE1 8ST, UK. E-mail: richard.fu@northumbria.ac.uk

<sup>b</sup> Department of Applied Physics, College of Science, Xi'an University of Science and Technology, Xi'an, 710054, P. R. China

<sup>c</sup> Shenzhen Key Laboratory of Advanced Thin Films and Applications, College of Physics and Energy, Shenzhen University, 518060, Shenzhen, P. R. China

<sup>d</sup> Institute for Multiscale Thermofluids, School of Engineering, University of Edinburgh, Kings Buildings, Edinburgh EH9 3FB, UK

<sup>e</sup> Division of Biomedical Engineering, James Watt School of Engineering, University of Glasgow, Glasgow G12 8LT, UK

<sup>f</sup> Key Laboratory of Micro and Nano Systems for Aerospace, Ministry of Education, North Western Polytechnical University, Xi'an 710072, P. R. China

<sup>g</sup> College of Mechanical and Vehicle Engineering, Hunan University, Changsha 410082, P. R. China

<sup>h</sup> Institute of Thin Films, Sensors & Imaging, University of the West of Scotland, Scottish Universities Physics Alliance, Paisley PA1 2BE, UK

<sup>i</sup> College of Information Science & Electronic Engineering, Zhejiang University, Hangzhou 310027, P. R. China

<sup>j</sup> School of Materials Science and Engineering, MOE Key Laboratory of Micro-Systems and Micro-Structures Manufacturing, Harbin Institute of Technology, Harbin 150001, P. R. China



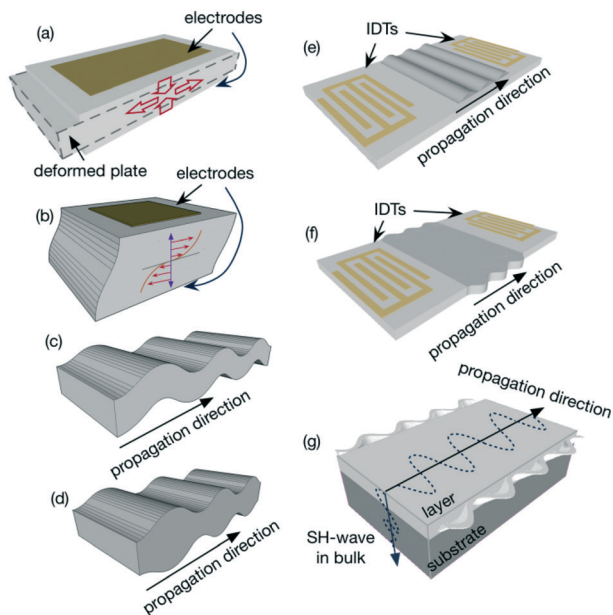


**Fig. 1** Illustrations of different types of commonly observed acoustic waves: (a) longitudinal bulk acoustic waves (BAWs) generated between a top electrode and bottom electrode; (b) thickness-shear mode (TSM) waves generated between two electrodes; (c) Lamb waves, antisymmetric mode (A mode, or flexural plate waves-FPWs); (d) Lamb waves, symmetrical mode or extensional mode (S mode); (e) Rayleigh surface acoustic waves (SAWs) generated on a piezoelectric material using interdigital transducers (IDTs); (f) shear horizontal SAWs (SH-SAWs) generated on piezoelectric materials using IDTs; (g) Love-mode waves generated on the surface of an SH-SAW device coated with a thin wave-guide layer.

recently been extensively studied. They have structures similar to those of BAW devices, but their dimensions (both size and film thickness) are much smaller (on the micron or sub-micron scale), thus achieving operation frequencies from sub-GHz to tens of GHz, suitable for high precision sensor applications.<sup>2,3</sup> Similarly, FBARs and SMRs can have either longitudinal or TSM waves, similar to those shown in Fig. 1a and b, depending on the crystal orientation of the film.

Lamb waves are commonly generated when the substrate thickness is smaller than or comparable to the wavelength of the propagating waves on the substrate (see Fig. 1c and d). Lamb waves include: antisymmetric mode (A mode), also called flexural plate waves (FPWs), and symmetrical mode or extensional mode (S mode). It has been recently reported that Lamb waves can be generated using thin film piezoelectrics on a membrane structure.<sup>4,5</sup>

In a surface wave configuration, interdigitated transducers (IDTs) are commonly deposited onto the piezoelectric material, and surface acoustic waves (SAWs) can be generated after resonant frequency signals are applied to these IDTs. The SAWs propagate on the surface of the material in either an out-of-plane (*e.g.* Rayleigh) mode or an in-plane (*e.g.*, shear horizontal) mode, as shown in Fig. 1e and f. Rayleigh SAWs can be generated on specifically oriented bulk piezoelectric substrates such as ST cut and Y-cut quartz, 128° Y-X-cut

LiNbO<sub>3</sub> and X-112° Y-cut LiTaO<sub>3</sub> substrates, as well as vertically aligned or (0002) oriented films (often called *c*-plane or *z*-plane orientated) of ZnO, AlN, PZT or LiNbO<sub>3</sub>. Shear-horizontal SAWs (SH-SAWs) are generated on ST-cut quartz, 64° Y-X-cut LiNbO<sub>3</sub> and 36° Y-X-cut LiTaO<sub>3</sub>, and the waves propagate *via* a shear-horizontal mode on the substrate surface<sup>6,7</sup> (Fig. 1f). SH-SAWs can also be generated on many piezoelectric thin films with in-plane textures such as (10 $\bar{1}$ 0) (commonly called the *m*-plane) or (11 $\bar{2}$ 0) (commonly called the *a*-plane), or (10 $\bar{1}$ 2) orientations (commonly called the *r*-plane).<sup>8–19</sup> Another commonly investigated SAW is Sezawa mode, which is excited in SAW devices that harbour a layered structure where the phase velocity of the SAWs in the substrate is much larger than that of the overlaid piezoelectric film.<sup>4,5</sup> They are intrinsically guided waves, which propagate at the interfaces between the film and substrate. The ratio of the wavelength to the piezoelectric film thickness plays a critical role in the properties of Sezawa waves. As the waves propagate along the interface, the influence of the structure of the thin film may be limited, although the detailed effects have not been studied.

Generally, bulk piezoelectric materials are much thicker and have better piezoelectric parameters on a large scale, whereas piezoelectric thin films have advantages in microscale devices for MEMS and lab-on-chip applications.<sup>2–6</sup> For a better understanding of the different film orientations of piezoelectric film materials, Fig. 2 shows four typically observed crystal orientations, *i.e.*, (0001) *c*-plane, (10 $\bar{1}$ 0) *m*-plane, (11 $\bar{2}$ 0) *a*-plane and (1 $\bar{1}$ 02) *r*-plane. Love mode SAWs, one of the key guided acoustic waves,<sup>20</sup> can be generated within a thin wave-guide layer (such as SiO<sub>2</sub>, ZnO or polymers with sub-micron thickness) coated onto an SH-SAW device as shown in Fig. 1g.<sup>21</sup> The Love mode waves have been regarded as optimal for biosensing under liquid conditions, mainly because the acoustic velocity of the wave-guide layer is lower

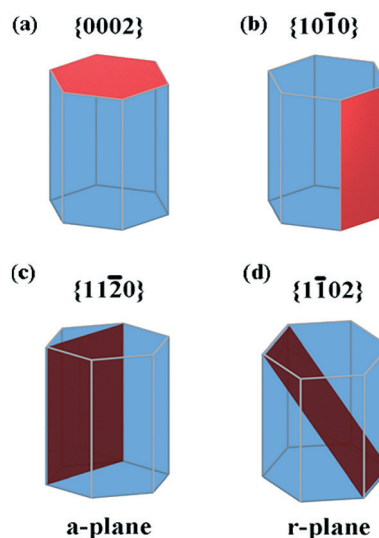


**Fig. 2** Illustrations of four commonly observed orientations for wurtzite piezoelectric crystal structures. (a) {0002} *c*-plane; (b) {10 $\bar{1}$ 0} *m*-plane; (c) {11 $\bar{2}$ 0} *a*-plane; and (d) {1 $\bar{1}$ 02} *r*-plane.



than that of the substrate; thus the SH-SAWs generated are mostly trapped within this thin wave-guide layer, leading to a high sensitivity to signal changes at the surface.<sup>22,23</sup>

Both the longitudinal bulk waves and out-of-plane (Rayleigh) SAWs are significantly damped when they come in contact with a liquid, because a large portion of their wave movements on the surface is vertical. Therefore, they are subjected to extensive damping, with significant deformations up to a few wavelengths at the solid-liquid interface. Therefore, they are not recommended for sensing applications in a liquid or highly humid environment, but instead have recently been extensively explored for acoustofluidic (or bio-sampling) functions such as mixing, jetting, nebulisations, particle/cell manipulations and acoustic heating.<sup>24–27</sup> TSM waves, SH-SAWs and Love mode waves have been applied for liquid sensing due to their limited dissipation of wave energy during their propagations at the solid-liquid interface, but for the same reason, they are less commonly used in acoustofluidics.<sup>28,29</sup>

Recently acoustic wave devices have been extensively explored for detection of biomolecules, viruses, DNA, bacteria and cells.<sup>4,5,30</sup> Most of these devices are required to work in a liquid environment. Therefore, there is a need to generate both shear waves (either TSM or SH-SAWs) for efficient bio-sensing and longitudinal or Rayleigh waves for bio-sampling and liquid sample manipulation processes, in one device platform. However, there are significant challenges to generate both these functions onto one single piezoelectric substrate with a given crystal orientation.

For the BAW devices, it is possible to generate both longitudinal and shear wave modes by fabricating devices on a bulk piezoelectric material with a suitably chosen crystal cut or orientation (*e.g.*, non-vertically aligned ones). Similarly, thin-film FBARs based on specially designed inclined angled piezoelectric ZnO and AlN thin films have been extensively investigated to generate both longitudinal (for microfluidics) and BSM waves (for liquid sensing) and thus have been used under liquid conditions as shown in Fig. 3a.<sup>31–35</sup> Generally the longitudinal wave has a higher frequency than the corresponding bulk shear mode due to their differences in acoustic wave velocities with an illustration shown in Fig. 3b.

For quartz-crystal based SAW devices, Rayleigh waves can be excited and then propagate along the X-cut direction on the 37° Y-cut quartz wafer, whereas the SH-SAW can be excited normal to the above direction. For thin film-based SAW devices, if the electrodes of the interdigitated transducers (IDTs) are deposited on top of inclined angled piezoelectric films as shown in Fig. 3c, both the Rayleigh SAW and SH-SAW can be generated. It is generally agreed that the SH-SAW has a higher frequency than the Rayleigh one as illustrated in Fig. 3d.<sup>36–39</sup>

Apart from using the inclined-angled or non-vertically aligned films, other potential methods have been proposed to generate waves for sensing under liquid conditions on vertically oriented (0002) materials or films. For example, one key and widely studied method is the use of a lateral field

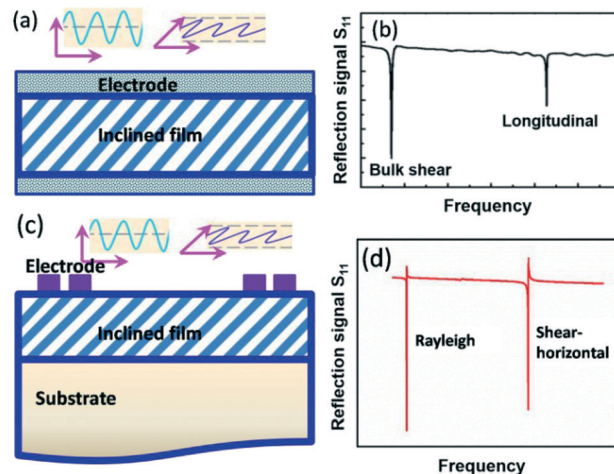


Fig. 3 The configurations of thin films and acoustic waves that can be generated: (a) thin film FBARs with inclined angled piezoelectric thin films can generate both longitudinal (for microfluidics) and bulk shear waves (for liquid sensing); (b) a schematic illustration to indicate the differences in the frequencies of longitudinal and bulk shear waves; (c) Rayleigh SAW and SH-SAW generated with IDTs deposited on top of inclined angled piezoelectric films; (d) a schematic illustration to indicate the differences in the frequencies of Rayleigh SAW and SH-SAWs.

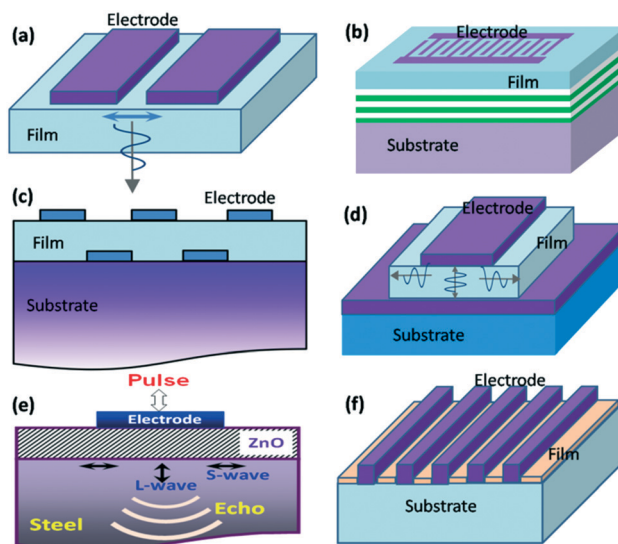


Fig. 4 The acoustic waves are excited in different structures: (a) lateral field electrode to form laterally excited ZnO or AlN thin film resonators to generate shear waves to be operated in a liquid solution; (b) tilt electric fields generated from standard IDTs on a *c*-axis vertically aligned piezoelectric film deposited on dielectric reflector stacks of AlN/SiO<sub>2</sub>, thus resulting in the electric fields being mainly aligned along the *x*-axis of the film plane; (c) the top and bottom electrodes are not perfectly aligned in the *z*-direction, thus the asymmetrical fields will generate both vertical and shear waves; (d) off-axis excitation, where the top electrode is relatively smaller than the bottom electrode; thus both pseudo-shear and pseudo-longitudinal waves can be generated; (e) both longitudinal wave (L-wave) and shear bulk wave (S-wave) generated in a standard pulse-echo ultrasonic test; (f) a periodically patterned ZnO film was deposited between fingers of IDTs to fill the gaps of the IDTs and implement SAW resonators.



electrode (LFE) design<sup>40–43</sup> as illustrated in Fig. 4a. This establishes laterally excited resonators to generate shear, or mostly pseudo-shear waves,<sup>44–47</sup> which can be used for biosensing in a liquid environment, along with vertical waves for acoustofluidic functions to form an integrated lab-on-a-chip based on thin films.<sup>48</sup> These types of LFE designs can be easily combined with FBAR or SMR designs, thus generating both longitudinal and shear thin film bulk modes.<sup>49</sup> For the LFE mode, the shape, dimension and distance of two electrode pads are not critical, whereas the thickness of the piezoelectric material below is critical to determine the generation of the wave frequencies.

Another method is to modify electric fields generated from standard IDTs (as shown in Fig. 4b and c). In Fig. 4b, a bulk shear acoustic wave can be generated using a standard IDTs on a *c*-axis vertically aligned piezoelectric film deposited on dielectric reflector stacks of AlN/SiO<sub>2</sub>, thus resulting in the electric fields being mainly aligned along the *x*-axis of the film plane.<sup>50</sup> Meanwhile, in Fig. 4c, the top and bottom electrodes are not perfectly aligned in the *z*-direction, thus the asymmetrical fields will generate both vertical and shear waves, although the film's crystal structure is vertically aligned.

Another method explored to a lesser extent is called off-axis excitation, where the top electrode is relatively smaller than the bottom electrode; thus both pseudo-shear and pseudo-longitudinal waves can be generated by this method as shown in Fig. 4d. A similar idea using two top electrodes with different areas has also been proposed for a ZnO SMR sensor, which can generate both shear and longitudinal modes for biosensing under liquid conditions.<sup>51</sup> This design is actually often reported in standard pulse-echo ultrasonic tests where a mixture of shear and longitudinal waves can be easily generated when using a small area of the top electrode on thin-film coated metallic substrates (see Fig. 4e).<sup>52,53</sup>

There is another reported method<sup>54</sup> in which a periodically patterned ZnO film was deposited between fingers of IDTs to fill their gaps and implement the SAW resonator as shown in Fig. 4f. Both the longitudinal and transverse wave modes can be generated.

However, the efficiency in generating strong and effective shear mode waves for all the above-mentioned unique designs is debatable.<sup>55,56</sup>

So far, the use of inclined angled thin films has been shown to generate both longitudinal (or Rayleigh waves) and TSM (or SH-SAW) waves. The produced inclined angled thin film devices can be used as the building blocks of integrated microsystems for microfluidic lab-on-a-chip, with the possibility of using separate wave modes for the functions of liquid transportation, biosampling and sensing. However, there are many contradictory views in the literature about the inclined angles of films (either columnar or crystal ones), the fundamental formation mechanisms of inclined crystals and their key growth parameters. Many different techniques have been developed but there are a lot of issues on uniformity of inclined angles, film thickness and acoustic wave properties. It is still a great challenge to successfully generate both these

types of waves for SAW and FBAR devices and realise all the different functions of an integrated lab-on-a-chip. In this paper, we address all of the above issues and discuss the following key questions:

- (1) What are the fundamental and theoretical issues in the use of inclined films to generate both vertical and shear waves?
- (2) How can inclined columnar and inclined crystal piezoelectric films be produced efficiently using film deposition methods and what are the key processing parameters?
- (3) How can both shear waves and longitudinal/Rayleigh waves be generated?
- (4) How can these waves be effectively integrated into one platform and applied for lab-on-chip applications?

## 2. Fundamentals of angles of inclination and wave modes in inclined films

SAW and FBAR devices based on inclined films have recently been extensively studied and have shown improved mass sensitivities and good performance under liquid conditions.<sup>57,58</sup> For these devices, the inclination angles have shown significant influences on the generation of acoustic wave modes.

### 2.1. Definitions of three angles of inclination

Before discussing the details of these mixed wave modes, three different definitions of the angles of inclination must be clarified, which have been previously discussed in ref. 4 and 5:

**a. Substrate inclination angle  $\alpha$ .** The first type of inclination angle has been defined as the substrate tilting angle. During deposition, the substrate can be tilted or inclined to the deposition source at a desired angle, which can be varied from 0° to 90°. Angle  $\alpha$  is sometimes also called the target-tilting angle if the target is adjusted into a certain angle when the substrate position is fixed. This angle is easily adjusted by the experimental design using deposition methods such as oblique angle deposition (OAD, see Fig. 5a) or glancing angle deposition (GLAD, see Fig. 5b).<sup>59</sup> During the OAD process, inclined columnar structures can be readily achieved by tilting/fixing the substrate at a large angle (normally much larger than 45°) in the direction of the incident flux. In the GLAD process, the substrate movements are precisely controlled (tilting/rotating in a 3D scheme at very large tilting angles) during the deposition, and the deposited films often show large inclined columnar angles with nanopillars, zig-zag or helical nanoscale patterns.<sup>60–66</sup>

**b. Columnar inclination angle  $\beta$ .** The second definition of inclined angle is the film's columnar inclined angle, and the exact values of angle  $\beta$  can be obtained from morphological analysis based on cross-section images of optical or electron microscopes. The columnar inclined angle  $\beta$  is generally smaller than the substrate tilted angle  $\alpha$ , as illustrated in Fig. 5c.<sup>67</sup> In some cases, there is no apparent inclined



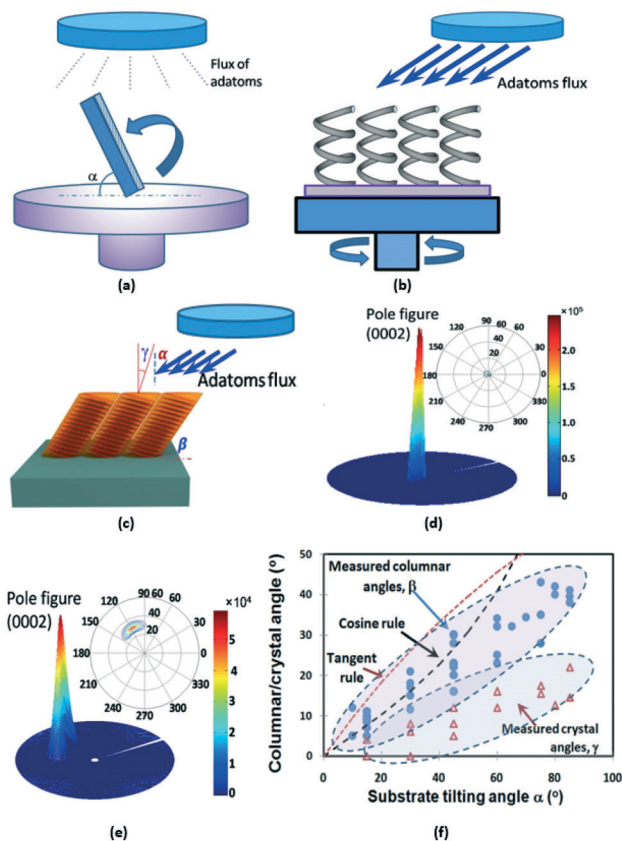


**Fig. 5** (a) Tilting angle deposition or oblique angle deposition (OAD); (b) glancing angle deposition (GLAD) with tilting/rotating in a 3D scheme at very large tilting angles; (c) illustration of the relationship between columnar tilting angles, substrate tilted angles and crystal tilting angles; (d) X-ray diffraction (XRD) pole figures of a *c*-axis orientated AlN film; (e) XRD pole figures of a 30° crystal inclined AlN film; both figures (d) and (e) are provided by Prof. Enrique Iborra from the University of Polytechnic Madrid, Spain; (f) different angle readings along with the data produced from the tangential and cosine rules.<sup>5</sup> Here, the adatoms refer to the arriving and deposited atoms/ions onto the substrate surface, and they are derived from the sputtering targets through diffusion, migration and bombardment.

columnar morphology (probably due to the formation of smooth and dense film microstructures) even after the substrate has been tilted significantly.

**c. Crystal inclination angle  $\gamma$ .** The third angle is defined as the film's crystal inclination angle,  $\gamma$ , which specifies that the crystal orientation is inclined at a certain angle to the (0002) plane of the films (see Fig. 5c). The crystal inclination angle  $\gamma$  can be determined using texture analysis methods such as X-ray diffraction (XRD) through pole figures or psi ( $\psi$ ) scan<sup>68</sup> (with examples of illustration shown in Fig. 5d for a (0002) vertically aligned AlN film and Fig. 5e for a 30° crystal inclined AlN film), or using a transmission electron microscope (TEM) with the help of electron beam scattering diffraction (EBSD). Another less commonly used method to characterise the tilting angle (mainly for AlN films) is to analyse the Raman peak position of the longitudinal optic

(LO) quasi-mode at  $\sim 890\text{ cm}^{-1}$ , whose shifts are linked to the *c*-axis crystal angle tilting at the surface of the film.<sup>69</sup>

Generally, the crystal inclination angle  $\gamma$  is much smaller than the columnar tilted angle  $\beta$  (see Fig. 5c and f). In many cases, even though the film shows a large columnar inclined angle, the crystal inclination angle is actually near zero, meaning that the crystals in the film still grow along the (0002) orientation.<sup>70</sup> However in other cases, the cross-section morphology did not show any apparent inclined columnar morphology, even after the film was deposited by significant tilting of the substrate. However, detailed texture analysis using X-ray diffraction (XRD) revealed the formation of crystal inclined structures.<sup>71</sup>

## 2.2. Relationships among angles of inclination

Empirical relationships have been proposed to analyse the links between the substrate tilting angle  $\alpha$  (or incident angle of the vapour flux) and columnar inclination angle  $\beta$  using the OAD method. For example, the tangent rule,<sup>72,73</sup> cosine rule<sup>74,75</sup> and other empirical equations are commonly used relationships:

$$\tan(\alpha) = 2 \tan(\beta) \quad (1)$$

$$\beta = \alpha - \arcsin[(1 - \cos \alpha)/2] \quad (2)$$

$$\tan(\beta) = 2 \tan(\alpha) / \{3[1 + \phi \tan(\alpha) \sin(\alpha)]\} \quad (3)$$

Fig. 5(f) shows the curves of substrate tilting angle  $\alpha$  as a function of columnar inclination angle  $\beta$ , predicted by both the tangent rule and cosine rule. Clearly both of these rules could not precisely predict the experimental data of sputtered deposited ZnO thin films especially at large substrate tilting angles (although it seems that the cosine rule shows a better prediction of data obtained at lower tilting angles). The reason for this difference is mainly because these proposed rules were developed based on the measurement data of thin films deposited using evaporation processes (in which a good “line of sight” property of vapour flux and a long distance between the evaporation source and substrate can be achieved due to low chamber pressures in the deposition process), while most of the piezoelectric films for the SAW and FBAR devices are prepared using sputtering methods. During sputtering processes, there are more random scattering effects<sup>4,5</sup> due to: (1) the shorter distance between the target and substrate; (2) varied target geometries (*e.g.*, rectangular or circular); (3) significant angular distribution of plasma sources. Therefore, the columnar inclination angles of the sputtered films may not be uniform or may not exactly follow the empirical rules developed from the data of evaporation processes, such as those obtained using eqn (1)–(3). It was also reported that the columnar inclined angles are also dependent on the film materials/chemistry<sup>76</sup> and substrate conditions (for example, texture or roughness of the substrate), which makes this a complex issue.



To the best of our knowledge, there are no available analytical relationships between the substrate tilting angle and crystal inclination angle ( $\alpha$  vs.  $\gamma$ ), or between the columnar inclination angle and crystal inclination angle ( $\beta$  vs.  $\gamma$ ). This is mainly due to the crystal orientation/angles being influenced by a wide range of parameters, including process parameters, thin film material properties, target and substrate conditions and properties. Fig. 5(f) shows some data of crystal inclination angle  $\gamma$  as a function of substrate tilting angles  $\alpha$  obtained from inclined angled ZnO and AlN films. Another challenge is that the XRD or TEM/EBS D methods are needed to precisely determine crystal orientations. However, these data are not widely available, partly because of the complexity of the geometry of the sample preparation and the speciality of the characterisation techniques. It is generally agreed that the crystal inclination angles are much smaller than the columnar angles, and in many cases, the  $c$ -axis crystal orientation (0002) is still dominant for most of the columnar inclined films. Another reason could be that the deposited “inclined” films are actually a mixture of vertically aligned crystals and inclined angled crystals, and it is difficult to develop mathematical models for the description of the relationships among the different angles (*e.g.*,  $\alpha$ ,  $\beta$  and  $\gamma$ ).

### 2.3. Key mechanisms determining columnar and crystal inclination angles

The columnar inclination angles are pre-dominantly controlled by deposition process parameters and substrate conditions. To generate columnar inclination angles in the films, the main controlling mechanisms include:

- (1) Direction and energy of the incoming adatoms on the deposited film;
- (2) Surface micro-/nano-scale features and their shadowing and self-shadowing effects;
- (3) Migration/diffusion of surface adatoms;
- (4) Channelling effect or momentum/bombardment of arriving adatoms.

On the other hand, crystal inclination angles  $\gamma$  in the deposited films are intrinsically determined by competing factors among the growth rates of different crystal orientations or crystal planes on the film surface,<sup>77,78</sup> which are controlled not only by process parameters, but also by material properties of both the film and the substrate. In the following, we will discuss a few key factors.

- Shadowing effect (mostly determines the columnar inclined angles).

During the OAD processes, the newly generated crystal nuclei on the substrate can form shadows behind them, which prevents the further formation of microstructures in these “shadowed” regions (see Fig. 6a), thus forming columnar inclined angle structures. This so-called shadowing effect is strongly linked to the directionality of the incoming particles. The inclined angled columnar structure is easily generated when the arriving particles have a good line of

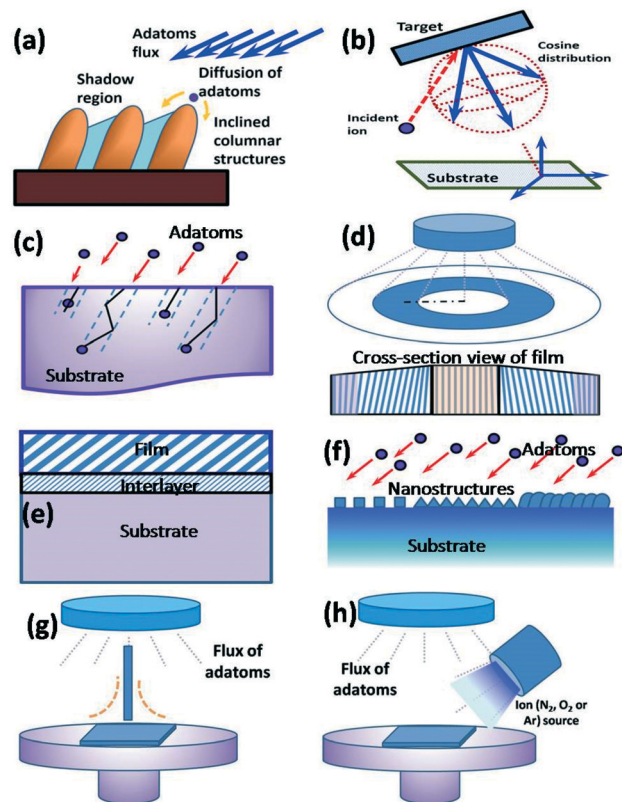


**Fig. 6** (a) Illustration of the shadowing effect during film deposition; (b) cosine law distribution of the sputtered adatoms on the substrate surface; (c) channelling effects during the sputtering process; (d) a circular-shaped target produces a ring distribution of inclined columnar angles (dark area) in the films, which can be revealed clearly from the illustration of the cross-section morphology; (e) an interlayer can promote the growth of inclined angled films; (f) pre-treatment of the surface to generate the desired surface roughness or surface topography and enhance the shadowing effect for growth of inclined angled films; (g) an additional blind/shutter positioned between the target and the substrates can change the plasma distribution onto the deposited films, thus promoting the inclined film growth; (h) an external oxygen or nitrogen ion or plasma source can control the oxygen/nitrogen ion bombardment to the deposited film during its inclined angled film growth.

sight such as in an evaporation process, and also if the substrate tilted angle is large enough. On the contrary, during the sputtering process, the plasma contains energetically charged ions, reactive species and sputtered atoms, which are all attracted onto the surface of the deposited film with different impinging angles. There is a well-known cosine law to describe the distribution of the sputtered adatoms as below (also illustrated in Fig. 6b):<sup>79</sup>

$$J(\theta) = Y\varphi(\cos \theta\pi) \quad (4)$$

where  $J(\theta)$  is the emission flux angular distribution as a function of the tilting angle  $\theta$  (*vs.* the vertical direction),  $Y$  is the sputter yield emitted from the surface, and  $\varphi$  is the local ion flux incident onto the surface. This cosine law distribution of sputtered adatoms will surely cause a more randomly



distributed flux of ions/adatoms (compared with a conventional evaporation process) through the discharge plasma, and thus less line-of-sight effect when the adatoms reach the substrate surface. These, unfortunately, may not contribute to generating a strong shadowing effect as preferred.

- Bombardment and channelling effects (for both columnar and crystal inclination angles).

During sputtering processes of ZnO, AlN and PZT films, various reactive species (such as O<sup>-</sup>, O, N, N<sup>+</sup>, N<sup>2+</sup>, etc.) and energetic species (such as Ar or Ar<sup>+</sup> ions) in the plasma have strong influences on the energy transfer to the deposited films. During a standard magnetron sputtering process, the kinetic energy of sputtered atoms/ions arriving at the substrate could vary from sub-eV to hundreds of eV, which generate various effects (such as deposition, bombardment, etching, and implantation) and have a significant effect on the formation of columnar structures. As will be explained later, process parameters, such as a higher plasma power or a lower pressure, will result in an increase of the kinetic energy of these impinging atoms onto the substrate, which is one of the key reasons why fully crystalline films and also piezoelectric effects of ZnO, AlN and PZT can be easily achieved in the sputtering process operated without any external heating, or post-poling processes.<sup>4,5</sup> Similarly, this effect would significantly influence the columnar inclined angles of the deposited film.

It is well-known that bombardment of the adatoms during sputtering will generate the so-called channelling effects (see Fig. 6c), which enhance the formation of columnar inclined structures, especially at a low incident flux and in a low temperature/pressure environment. In such circumstances, free movement of adatoms (deposited onto the substrate surfaces) can be restricted in a certain direction, thus promoting film growth along a desired orientation. For example, the (10 $\bar{1}$ 0) plane was found to be easily generated when the film was exposed to ion irradiation during electron beam evaporation due to its line-of-sight effect.<sup>80</sup> During deposition of ZnO and AlN films, the film texture was changed from (0002) into (10 $\bar{1}$ 0) or (11 $\bar{2}$ 0) by using a directional oxygen or nitrogen ion beam placed at an angle to the substrate surface, which is mainly due to this ion channelling effect.<sup>81</sup>

- Surface migration/diffusion (for both columnar and crystal inclination angles).

Irradiation or bombardment of the arriving adatoms could contribute to the densification of the film's microstructure by enhancing the mobility of the deposited adatoms through the angular distribution of the neutral species.<sup>82</sup> During the sputtering process, ion bombardment (mainly Ar, as well as O<sub>2</sub> or N<sub>2</sub>) will significantly influence the structures of the crystals, as well as the development of large compressive stress,<sup>83,84</sup> and could result in either formation of dense microstructures (due to the enhanced mobility of the deposited adatoms), or porous structures (due to the channelling effect or bombarding/damaging effects). In many cases, significant surface migration of adatoms deposited onto the film surface is not effective to promote the crystal inclined angle formation.

- Nature of the film material and bonding probability (mostly for crystal inclination angles).

Crystal angles of films are linked with the nature of film materials and also different bonding probabilities of atoms during growth. For example, for an AlN film, this factor could link to the formation of bonds such as (N, Al) or dimers (Al-N).<sup>85</sup> It was reported that a higher chamber pressure promotes the generation of more (Al-N) dimers thus resulting in the growth of AlN (10 $\bar{1}$ 0) planes. Meanwhile, at a low pressure, atoms of N and Al are dominant, rather than the dimers of Al-N, and thus the (0002) growth is promoted.<sup>73</sup> The effects of pressure will be discussed in the next section.

#### 2.4. Effects of sputter deposition process parameters

As discussed above about the physical mechanisms, the energy/angular distribution of the incoming material flux and the mobility of the adatoms during the inclined angled deposition process are critical for the formation of film microstructures. All sputter deposition process parameters will influence the film growth in different orientations and the surface mobility of adatoms and thus will influence the inclination angle of the film growth.<sup>76</sup> These key process parameters include:<sup>4,5</sup> the nature of the substrate (such as phases or chemical composition, crystalline orientation, roughness, etc.) and process parameters (such as gas pressure, target plasma power, position and distance of the substrate vs. target, deposition time, bias potential, substrate temperature, gas ratio and flow rates, external ion/electron beam source, and plasma shields).<sup>86</sup>

**2.4.1. Plasma power and substrate bias voltage.** In sputtering processes, the target power affects the energy and mobility of the adatoms when they arrive at the substrate. Increasing the target power will increase the kinetic energy of the adatoms arriving at the substrate, thus enhancing both the channelling effect and surface migration/diffusion effect (see section 2.3). However, the effect of target power is quite complex. For example, an increase of the target power increases the deposition rate, and the fast arrival of the adatoms on the film surface quickly buries the previously deposited ones, causing the formation of loose or columnar microstructures.<sup>87</sup> Excessive target power causes structural damage, resulting in the formation of coarse columnar structures in the films. Meanwhile a high target power can also generate high kinetic energy, thus bombarding the film surface and enhancing the surface diffusion, which might densify the deposited film and prevent the formation of columnar structures.

When an external bias voltage/power source is applied to the substrates during the sputtering deposition, the film orientation along (0002) is generally enhanced, but not the other orientations due to the normal direction of the energetic Ar ions bombarding onto the substrate surface. During the growth of ZnO and AlN films, a positive bias has been shown to increase the kinetic energies of oxygen or nitrogen ions, and enhance the mobility of adatoms arriving onto the film surface, causing significant bombardment/



cleaning effects, large compressive stress and increase in roughness. A negative bias decreases bombardment but still provides sufficient mobility of adatoms arriving onto the film surface, thus enhancing (0002) texture growth.<sup>4,5</sup>

**2.4.2. Target geometry.** As mentioned, the sputtering target is normally placed close to the substrate (compared with the evaporation process, for example), thus the atoms/ions which are sputtered away from the target reach the substrate along a wide range of directions due to the angular distributions of ions or scattering in the plasma. Positioning the substrate away from the sputtering target could produce clearer columnar inclined films, but at the expense of reduced energy of arriving adatoms on the substrates and poor crystallinity.<sup>88</sup> The shape of the target also shows a significant influence on the uniformity of the inclined angled films. For example, a circular-shaped target produces a circular ring region of inclined columnar angles in the films (as illustrated in Fig. 6d), but the central areas directly below the target and the areas far away from the targets could still show the vertical columnar structures due to the energy distribution of the arriving deposited adatoms, which we will discuss in a further section.

**2.4.3. Gas pressure and gas flow rate.** The gas pressure and gas flow rate have been shown to not only determine the mean free path of sputtered adatoms, but also influence the plasma density on the target.<sup>76,85,89,90</sup> A low chamber pressure (for example, below 1 mTorr) is often required to generate significant ion bombardment (from atoms/ions of argon, oxygen and nitrogen) and provide a longer mean free path to preserve adatom energies and reduce gas-particle scattering.<sup>91</sup> This enhances the channelling effects and promotes the formation of inclined columnar angles. At a high chamber pressure (for example, tens of mTorr), the sputtered particles can experience a large number of collisions in the chamber before arriving at the substrate and this reduces the kinetic energy and momentum (including the direction of arrival angles) of the sputtered particles upon reaching the film surface. Therefore, a high chamber pressure could decrease the adatom mobility and increase the shadowing effect, and thus could also be beneficial for the formation of columnar inclined films. For example, it was reported that the inclined crystal angle was increased by up to 10° with the increase of gas pressure.<sup>88,92</sup>

O<sub>2</sub>/Ar or N<sub>2</sub>/Ar gas ratios also have significant effects on the film texture.<sup>93</sup> For example, AlN films with (10 $\bar{1}$ 0) or (11 $\bar{2}$ 0) orientation were obtained on 3C-SiC-on-Si substrates by simply increasing the nitrogen to argon ratio from 40% to 80% at a total gas flow of 50 sccm.<sup>84</sup> In this case, the variations of the gas ratio would change the kinetic energy of the atoms deposited onto the films.

**2.4.4. Substrate temperature.** Substrate temperature during deposition has been shown to provide a way to control both columnar and crystal inclination angles. Heating the substrate changes the microstructures of the deposited film due to an increase in the mobility of adatoms, which could promote (0002) oriented film growth rather than crystal

inclined film growth such as that reported for AlN films.<sup>94</sup> Deniz *et al.*<sup>95</sup> reported that there is a temperature threshold, above which surface diffusion of the adatoms becomes dominant over surface shadowing, thereby preventing the formation of a typical inclined angled columnar feature.

**2.4.5. Substrate effect: composition, orientation, interlayer, and surface features.** Epitaxial growth of films with various orientations on different substrates has previously been explored using methods such as molecular beam epitaxy (MBE), metal organic vapour phase epitaxy (MOVPE), or laser processing,<sup>96–100</sup> on certain orientations of common substrates such as quartz, sapphire, LiNbO<sub>3</sub>, SrTiO<sub>3</sub>, diamond, MgO, CaF<sub>2</sub>, GaAs, GaN, GaN/sapphire and SiC. Examples include ZnO(11 $\bar{2}$ 0)//LaAlO<sub>3</sub>(100),<sup>101</sup> ZnO(11 $\bar{2}$ 0)/*r*-plane (10 $\bar{2}$ 2),<sup>102</sup> and ZnO(11 $\bar{2}$ 0)/sapphire Al<sub>2</sub>O<sub>3</sub>(01 $\bar{2}$ 2).<sup>103</sup> However, these epitaxial growth methods are expensive and the orientations are significantly dependent on the quality of the substrate materials and deposition conditions.<sup>16,103</sup>

Another commonly used method for changing the film orientation is to deposit an interlayer or a seed-layer (as illustrated in Fig. 6e), which could provide a template and promote the inclined angle growth of the piezoelectric films.<sup>104,105</sup> For example, a thin AlN buffer of tens of nanometres has significantly facilitated the crystal quality of *a*-plane ZnO films and the formation of SH-SAWs.<sup>106</sup> This type of interlayer does not need to be a piezoelectric material. This interlayer can be further pre-treated to generate the desired surface roughness or surface topography and enhance the shadowing effect in order to grow columnar inclined angled films (see Fig. 6f for some examples of these patterns). For example, a ZnO film with an inclined angle of 45° was obtained on a diamond substrate<sup>107</sup> with pre-deposited pyramidal-shaped diamond features,<sup>108</sup> mainly due to shadowing effects. Pre-patterned substrates can be prepared using a variety of methods, including photolithography, ion-beam milling, laser beam writing, nano-imprinting, embossing and self-assembly of nano-structured array patterns.

### 3. Sputtering techniques and technical challenges

In this section, we will discuss further about the sputtering techniques and challenges to realise different types of inclined films.

#### 3.1. Substrate tilting or target tilting

As mentioned, inclined ZnO and AlN films are commonly prepared using the OAD method.<sup>81,109–114</sup> The setup and process of the OAD method are simple, through either tilting the substrates, or sometimes tilting the target. However, the uniformity is critical, and the inclination angles and film thicknesses could be dramatically different along the substrate plane, which causes a big problem for massive production and device performance. Also nanorods or helical structures of ZnO or AlN can easily be grown using the OAD or GLAD method.





However, high-performance SAW and FBAR devices have not been generated from these highly porous nanostructures, due to high dissipation of energy for effective wave propagation.

### 3.2. Locating samples at off-centre positions<sup>115</sup>

In the sputtering process, if the target is small compared with the substrate, a deposited film has a vertically columnar structure and (0002) orientation at its centre area as shown in Fig. 6d as an example. At a certain distance away from the target (or at off-centre positions from the plasma source as shown in Fig. 6d), inclined angle columnar structures with tilted angles up to 10° to 20° can be obtained, mainly due to ion channelling and shadowing effects.<sup>116</sup> However, at locations far away from the plasma source, the (0002) orientation becomes dominant again as illustrated in Fig. 6d, mainly due to the limited ion/electron/atom bombardment energy and insignificant channelling effects, leading to the dominant self-orientation along the (0002) orientation. This simple technique is believed to avoid the need for any special re-configuration of the deposition setup. However, the window area over which a uniformly inclined angle is produced is quite small (for example, a circular and ring area as shown in the dark area in Fig. 6d). This surely poses a challenge for the mass production of acoustic wave devices.

### 3.3. Epitaxial growth on a specific substrate

Generally, by selecting a suitable substrate with a preferred orientation, inclined crystal films can be deposited using specific methods. However, these process methods are generally expensive, complicated, and difficult to control, as already discussed in section 2.4.5.

### 3.4. A suitable seed layer with inclined angles

Inclined films can be obtained when they are grown onto a pre-deposited seed layer with a texture or pre-fixed inclined angle on the substrate. For example, using a textured Al film as a seed layer, tilted crystal ZnO films have been developed for liquid sensors.<sup>108</sup> Using an AlN (2 $\bar{1}$ 19) orientation seed layer, inclined angled ZnO films with a *c*-axis crystal inclined at angles up to 45° have also been successfully obtained. The inclined crystal AlN seed layer enhanced the coupling coefficients of the ZnO films and achieved narrower angle distributions in the inclined crystal film.<sup>117–120</sup> Technically this (2 $\bar{1}$ 19) AlN seed layer could be obtained using a sputtering method with a low sputtering power and a relatively high pressure.<sup>120</sup> More details have also been discussed in section 2.4.5.

### 3.5. Using a shutter or blind placed between the target and substrate

An additional blind/shutter (for example, a metallic plate) can be placed between the target and the substrates and thus only allows oblique particles to arrive on the substrate surface (see Fig. 6g).<sup>121</sup> The changes of plasma distribution near the shutter

or blind enhance the ion bombardment/channelling and shadowing effects.<sup>122</sup> This type of blind shutter can also be designed to move horizontally or rotated into different tilting angles, thus the distributions of plasma onto the substrate would be changed, thus realising different columnar angled films. However, the obtained area is relatively small and the uniformity of inclined angled films is often poor.

### 3.6. External ion or electron beam sources

An external oxygen or nitrogen ion beam source can be used to control the oxygen/nitrogen ion bombardment during film growth as illustrated in Fig. 6h.<sup>123</sup> These sources, including an ion beam, an external electric field,<sup>124</sup> or an additional anode located near the substrate, can have a significant effect on the orientation of the growing films based on ion channelling effects,<sup>37</sup> as discussed in section 2.4.1. This generally makes the deposition process complicated and high cost, and the treated area of the film is not large, which is mainly dependent on the size of ion beam sources.

### 3.7. Summary of technical challenges

Even though inclined angled films as thick as a few microns (see Fig. 7(a) for an example) with a size of a four inch wafer have been successfully prepared using different techniques during the sputtering deposition, there are still many critical issues to be solved:

(1) Non-uniformity of film thickness and inclination or tilting angles over a large planar scale. As mentioned, most of the methods used to generate the inclination angle are not able to obtain a significant uniformity over large areas (for example, larger than 2 or 3 inches);<sup>125</sup>

(2) Variation of inclination angles along the film's cross-section (*e.g.*, thickness) direction. It is a challenge to maintain a constant inclined angle along the thickness direction. Studies showed that the columnar inclination angles of films would

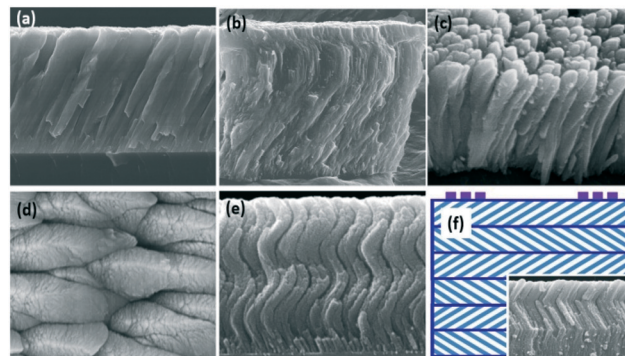


Fig. 7 (a) Inclined angled ZnO films with a thickness of 3.5 microns on silicon; (b) the columnar inclination angle of films has gradually changed during deposition; (c) porous and loose columnar inclined microstructures; (d) rough and significantly elongated surface grainy structures for columnar inclined angled ZnO films; (e) example of 3D spiral and porous titania nanorod structures fabricated from the GLAD method; (f) illustration and example of multi-layered zig-zag ZnO structures.



often be gradually changed during deposition, or sometimes even change to a vertical orientation during deposition (see Fig. 7b for an example).<sup>81,126</sup> These phenomena can be explained by the inevitable minor changes in the deposition conditions occurring over a lengthy deposition process (in most cases tens of hours), which could change the mobility of deposited species.

(3) Significant variations in acoustic wave propagation characteristics in planar directions. The large variation in *c*-axis tilt angles over a large area causes difficulties in obtaining consistent resonant frequencies and repeatable performance when a number of resonator chips are fabricated over this area. The acoustic wave velocities and frequencies of the devices decrease with increasing angles of inclination.

(4) A mixture of *c*-axis and inclined crystals in the deposited film. It is commonly seen that for the prepared inclined films, XRD analysis reveals that the film actually consists of both *c*-axis and crystal inclined films. This is probably the reason why many characterisation data of crystal inclined angles are confusing. However, identification of the precise percentages or ratios between them would be a challenging work.

(5) Formation of loosely columnar, porous or nanofiber structures due to self-shadowing effects. When the film is deposited at very large substrate tilting angles (*e.g.*, above 60° or 70°), the formed columnar microstructures are normally quite porous and loose (see Fig. 7(c)), and many film surfaces are very rough with a significantly elongated grainy surface morphology (see Fig. 7(d)). Indeed, both the OAD and GLAD methods have been mainly used to generate nano-pillars, nanorods or 3D spiral porous structures (see Fig. 7(e) for an example). Tait<sup>127</sup> derived an equation about the density of the film,  $\rho$ , as a function of the substrate tilting angle,  $\alpha$ .

$$\rho = 2 \cos \alpha / (1 + \cos \alpha) \quad (5)$$

The above equation clearly shows that the density of the deposited film decreases significantly with an increase of the tilting angle. The resulting rough surfaces and low density for the inclined angled films significantly reduce the *Q* factor of the resonant peaks of the devices due to the formation of surface defects such as etch pits, pyramids, ridges, and ledge-like and elongated grain structures. The potential spaces between columnar structures will cause elastic abnormality and anisotropy of the films.<sup>2</sup> Therefore, acoustic wave devices made of these films with very large columnar inclined angles often exhibit weak signals and low *Q* factors, *i.e.*, poor reflection and transmission performance.<sup>128</sup>

It should also be noted that one of the key advantages using piezoelectric films for acoustic wave devices is the generation of in-plane isotropic acoustic wave properties,<sup>4,5</sup> so the patterning positions or directions of IDTs or electrodes will not affect the wave mode generation and acoustic wave properties (such as velocities or frequencies). However, if columnar and crystal inclined films are used, the anisotropic acoustic wave properties within the film plane negate this benefit, *e.g.*, becoming significantly anisotropic.

(6) Poor film adhesion for porous and nano-columnar structured films at large inclination angles. Highly inclined columnar angled films generally do not have as good adhesion as vertical and dense films, although the film stress could be decreased significantly at a larger columnar tilting angle.<sup>129</sup> The lower film stress is mainly due to the formation of defects which cause tensile stress and are compensated for by film compressive stress.

In order to solve the issue of poor thickness uniformity, zig-zag (or spiral) patterns have been prepared by repeatedly changing the tilting angles of substrates (or by rotating the substrates) during tilted angle deposition.<sup>129–133</sup> By using multi-layered zig-zag structures as shown in Fig. 7f, the longitudinal mode was found to be significantly suppressed, whereas the shear mode was not affected.<sup>130</sup> The operational frequency and absolute sensing sensitivity in the liquid have also been reported to increase with layer numbers.<sup>132</sup> This means that the FBAR or SAW devices made of these multi-layered zig-zag films should significantly enhance the performance of the shear waves. The uniformity of the thickness of inclined films could also be improved if compared with one single inclined film.<sup>131,134</sup> Although in principle, this zig-zag film can be easily achieved using OAD and GLAD methods, the process increases the complexity of wave mode generation and device fabrication, and the microstructures become much poorer whilst the surface roughness is increased dramatically, all combining to pose significant challenges for its applications.

## 4. Effects of the inclination angle on wave propagation

### 4.1. On thin film bulk acoustic waves

Inclination angles (both columnar and crystal lattice) have significant effects on peak amplitude ratios between shear and longitudinal wave modes and their electromechanical coupling coefficients.<sup>134</sup> However, it should be noted that for most theoretical studies, the crystal inclined angle  $\gamma$  was used in the analysis, whereas for most of the experimental studies, the columnar inclined angle  $\beta$  was often used in the data analysis.

Fig. 8a and b show the theoretical values of wave velocities of both longitudinal and bulk shear modes of an AlN film as a function of crystal inclined angles, respectively, which follows the results proposed in ref. 134. As shown in Fig. 8a, the velocity of longitudinal wave decreases quickly with the increase of the inclination angle to ~45°, above which it increases slightly until 90°. Meanwhile, as shown in Fig. 8a, the velocity of bulk shear waves increases continuously with the increase of the inclination angle to 35°, above which it gradually decreases until 90°. Fig. 8b shows the electromechanical coupling coefficients of the AlN film as a function of the *c*-axis inclination angle for the bulk acoustic waves (including FBARs). When the inclination angle is increased from 0 to 45°, the ratio of shear wave mode (to the longitudinal one) and its  $k^2$  values gradually increase, whereas those of the longitudinal mode gradually decrease.



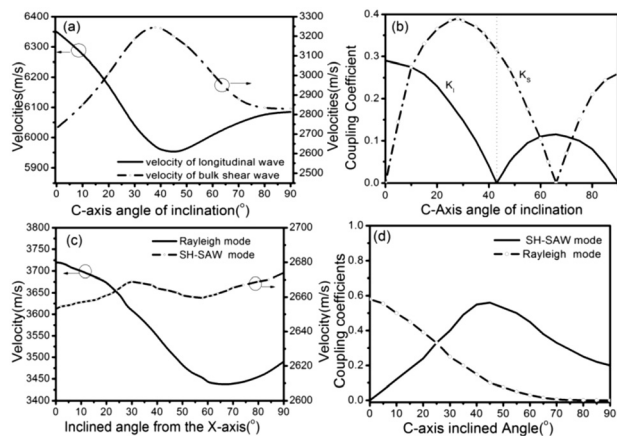


**Fig. 8** (a) Theoretically calculated wave velocities between longitudinal and bulk shear modes; (b) electromechanical coupling coefficients for both shear and longitudinal modes as a function of *c*-axis inclined angles for the FBAR devices; figures are redrawn and modified based on the results from ref. 134 and 138; (c) theoretically calculated wave velocities between Rayleigh and SH-SAW modes; (d) electromechanical coupling coefficients for both Rayleigh and SH-SAW modes as a function of *c*-axis inclined angles for the SAW devices. Figures are redrawn and modified based on the results from ref. 139, 140 and 143.

The values of  $k^2$  for the shear and longitudinal waves become similar at an angle of  $\sim 10^\circ$ . The  $k^2$  values of the shear mode become larger than the longitudinal values with the angle increased from  $\sim 10^\circ$  to  $\sim 60^\circ$ .<sup>135–137</sup> The maximum  $k^2$  value of shear mode resonance occurs at a *c*-axis angle of inclination of about 25–38°. Theoretical analysis shows that pure thickness-longitudinal modes for ZnO (or AlN) FBARs are generated at *c*-axis angles of 0° (0°) and 67.1° (65.4°), whereas pure thickness-shear modes for ZnO (or AlN) FBARs are generated at 43° (46.1°) and 90° (90°).<sup>134,138</sup>

Pang *et al.* studied the effect of inclination angles using a pulse-echo ultrasonic method<sup>141,142</sup> for inclined ZnO films with different columnar inclination angles on steel substrates. Results showed that both the longitudinal echoes and shear echoes from the back wall of the steel plate could be obtained. A dual mode wave pattern (*i.e.*, with both components of longitudinal and shear waves, mainly due to the small size of the top electrode compared to that of the metal substrate) was detected for the ZnO film with a crystal inclined angle of 0°. When the inclined columnar angle was increased, the amplitude ratios of the shear/longitudinal wave components were increased. When the inclined angle was increased to 31°, a nearly pure shear wave was obtained whilst the longitudinal wave excitation was significantly suppressed.<sup>141</sup> For further increases of the inclination angle up to 35°, the shear wave was still dominant but the longitudinal component re-appeared.<sup>141</sup>

#### 4.2. On SAWs

Reports on the effects of the inclination angle on the generation of Rayleigh mode and SH-SAWs are less readily

available. This is mainly because a relatively thicker inclined film with a larger scale of uniform inclination angle is required for the generation of these SAW modes, and the IDTs for the SAW devices generally have larger sizes (for example, in many cases the dimensions of their reflectors are added). Fig. 8c shows the velocity results of Rayleigh and SH-SAW modes as a function of the inclined angle vs. X-axis in bulk LiNbO<sub>3</sub> SAW devices. When the inclined angle is increased from 0° to 90°, the theoretically calculated velocity of the Rayleigh mode is much lower than that of the SH-SAW mode.<sup>139,140</sup> A similar dispersive behaviour of the Rayleigh and SH-SAW modes exists in the inclined piezoelectric films.<sup>136</sup> Fig. 8d illustrates that when the crystal inclined angle  $\gamma$  is 0° (*e.g.*, (0002) orientation) for the ZnO SAW devices, the Rayleigh wave is dominant and has the largest value of  $k^2$ . With an increase in crystal inclined angle  $\gamma$ , the value of  $k^2$  for the Rayleigh wave gradually decreases until becoming negligible as the crystal inclined angle approaches 90°.<sup>143</sup> Conversely, the amplitude ratio and  $k^2$  value of the SH-SAW peak become zero for vertically aligned films, but they increase with the crystal inclined angles up to 45°, and then gradually decrease up to 90°.

Yanagitani and Suzuki<sup>144</sup> reported that *c*-axis inclined AlN films showed significant decreases in shear wave acoustic impedance, but not in that of the vertical Rayleigh type of waves. They have attributed this effect to the significant shear elastic softening caused by the weak inter-columnar connection. This elastic softening effect could also explain the difficulties in achieving the SH-SAWs in inclined films, and there are few papers about the successful generation of both wave modes in inclined films.

## 5. Sensing, acoustofluidics and integrated lab-on-a-chip using inclined films

### 5.1. FBAR liquid sensors and microfluidic devices based on inclined angled films

Recently, FBAR or SMR sensors with inclined angled piezoelectric films have been extensively studied for biosensing in liquid. These sensors could be made from both ZnO and/or AlN films with columnar inclination angles and crystal inclination angles to generate shear waves for sensing in liquid.<sup>144–148</sup> The inclined angled films used in the fabrication of the FBAR or SMR devices are easily obtained as they are generally very thin (sub-microns to one or two microns) and small (*e.g.*, micron scale). Within such a thickness range and such an area range, a uniform inclined angled film in both thickness and planar directions is readily obtained, enabling a huge number of successful reports on their applications. Both ZnO and AlN films have been extensively used in these FBAR or SMR devices for biological applications in liquid environments as summarized in Table 1. Due to their much higher wave



propagation velocities for AlN films compared with those for ZnO films, AlN FBARs or SMRs have their advantages compared with those of ZnO devices, but the ZnO film has its advantages with relatively higher electro-coupling coefficients.<sup>149</sup> To further enhance the sensitivity and performance of FBAR devices, new materials, such as carbon nanotubes and graphene, were also deposited onto the inclined AlN film.<sup>150</sup>

As discussed above, inclined angled FBAR devices have been widely used in liquid biosensing, whereas so far, there are no reports for liquid actuation applications using the inclined angled FBAR devices. The integrated functions for both microfluidics and biosensing on one platform have never been demonstrated. In principle, bulk acoustic waves are able to generate liquid streaming and create flow patterns. For example, a circularly self-focused bulk wave acoustic transducer capable of generating focused waves on a (0002) oriented ZnO film on silicon, so-called “liquid needles”, was used to generate a focused acoustic wave in a liquid chamber and to produce a needle-shape liquid column on the free surface of the liquid tank.<sup>169–172</sup> Meanwhile, for many microfluidic functions, the electrical power required is quite high, thus the devices could be easily damaged, unless this has been controlled using methods such as compensation circuits.

## 5.2. Inclined angled SAW liquid sensors and microfluidic devices

Pure SH-SAW devices using films of the (10 $\bar{1}$ 0) *m*-plane, (11 $\bar{2}$ 0) *a*-plane and (1 $\bar{1}$ 02) *r*-plane, as well as Love mode thin film SAWs have been obtained in many configurations. However, there are few reports for successful achieving both Rayleigh SAW and SH-SAWs using one inclined angled piezoelectric film. It is still a great challenge to generate the integrated SH-SAW and Rayleigh waves for both microfluidics and biosensing by using inclined ZnO and AlN films, and this has never been reported so far.

Fardeheb-Nammeri *et al.*<sup>173</sup> previously reported that SAW devices made from *c*-axis inclined AlN films (with a maximum crystal inclined angle of 10°) achieved shear waves with a velocity of 5832 m s<sup>-1</sup>, and Rayleigh waves with a much lower velocity of 5082.72 m s<sup>-1</sup>. SH-SAW devices were also demonstrated using *c*-axis tilted Sc doped (44%) AlN films (*c*-axis inclined 5.5° over the whole sample surface) fabricated on sapphire.<sup>174</sup> Within these limited reported references, the SH-SAWs from the inclined film SAW devices have been applied for liquid sensing demonstrations, and the Rayleigh SAW components have never been used for microfluidics or biosampling demonstrations.

**Table 1** Summary of film bulk acoustic resonators (FBARs) and solidly mounted resonators (SMRs) based on inclined angled ZnO and AlN films for biosensing applications

Piezoelectric materials	Structures	Inclined angle	Working frequency	Sensitivity	Key applications	Ref.
ZnO	FBAR		2 GHz	2.4 kHz cm <sup>2</sup> ng <sup>-1</sup>	Detect DNA and protein molecules	151
ZnO	FBAR	16°	830 MHz	1 kHz cm <sup>2</sup> ng <sup>-1</sup>	Water-glycerol solution	152
ZnO	FBAR		1.04 GHz	500–1358 Hz cm <sup>2</sup> ng <sup>-1</sup>	Blood proteins ( <i>e.g.</i> A1b, IgG and fibrinogen)	153
ZnO	SMR	<i>C</i> -axis inclination angle 25°	1.1 GHz	4.9 kHz cm <sup>2</sup> ng <sup>-1</sup>	Rabbit immunoglobulin G (IgG) molecule	104
ZnO	FBAR		1.4 GHz		Human blood coagulation process	154–156
ZnO	FBAR		800 MHz	50 ppm	CO <sub>2</sub>	157
ZnO		13.6° tilted <i>c</i> -axis	1.28 GHz			158
ZnO	FBAR	<i>c</i> -axis inclined angle of 24°	2.26 GHz	20 pg ml <sup>-1</sup>	Cardiac biomarkers in the clinical serum	159
AlN	FBAR	<i>c</i> -axis 23°		800 Hz cm <sup>2</sup> ng <sup>-1</sup>	Human IgE	160
AlN	FBAR	30°	700 MHz to 1.5 GHz	1.5 to 2.9 kHz cm <sup>2</sup> ng <sup>-1</sup>	Streptavidin and biotinylated BSA, and crosslinked fibrinogen	161, 162
AlN	SMR	Crystal inclined angle of 30°	1.2 GHz			163
AlN	FBAR	20° columnar inclined	1.2 GHz	2045.89 Hz cm <sup>2</sup> ng <sup>-1</sup>	Carcinoembryonic antigens (CEA)	164
	FBAR	23°-Tilted columnar structure	1.175 GHz	1.425 × 10 <sup>5</sup> cm <sup>2</sup> g <sup>-1</sup>	IgE	165
AlN	FBAR	Inclined angles of 23°	1.17 GHz and 2.07 GHz	2295 Hz cm <sup>2</sup> ng <sup>-1</sup> , and 1363 Hz cm <sup>2</sup> ng <sup>-1</sup>		166
AlN	Shear mode SMR		1.3 GHz	1800 kHz pg <sup>-1</sup> cm <sup>-2</sup>	Gravimetric biosensor	57
AlN	FBAR	21.6° crystal inclined	1.87 GHz (6221 m s <sup>-1</sup> ) and 3.15 GHz (10 268 m s <sup>-1</sup> )		Human haemostatic parameters, such as prothrombin time (PT)	167, 168



As explained in section 3.7, the specific challenge related to the generation of both Rayleigh waves and SH-SAWs using the inclined angled films is the need for thick (a few microns) and large-area films (2 or 3 inch and above) in order to pattern the IDTs and precisely control the waves. Most of the films deposited using the OAD method have mixed *c*-axis and inclined crystals, and often the *c*-axis orientation is more dominant for the film texture. In most cases, due to the formation of loosely columnar, porous or nanofiber structures, the SH-SAWs in the inclined angled film devices show weak signals.

## 6. Conclusions and future outlook

This paper reviews the mechanisms, techniques and problems about inclined-angled piezoelectric films to generate both longitudinal (or Rayleigh) waves and thickness-shear bulk (or shear-horizontal surface acoustic) waves. This approach is advantageous, yet challenging, for simultaneously enabling molecular sensing and liquid actuation. So far, the generation of different wave modes has been demonstrated using inclined piezoelectric thin films with FBAR and SAW structures using three different types of inclinations: substrate tilting, columnar tilting, and crystal tilting. The effects of the inclination angle design should be evaluated carefully by identifying the specific definitions of these different angles. Applications of different types of waves integrated into lab-on-chips for multifunctionality have been explored. However, there are still technical challenges such as non-uniformity of the inclination angle and non-uniformity of the film thickness that limits their widespread adoption. The inclined films are generally relatively porous, have rough surfaces with poor adhesion, and generally do not retain usable acoustic wave properties for their application to real-life systems.

Recently there were also many studies for wearable and flexible SAW devices, in which thin foils of metal and polymers are used. When inclined films are deposited on thin substrates and foils, the control of foil deformation and the generation of different waves become challenging. In that case, Lamb waves or flexural waves will be dominant and co-existed with shear waves; thus the modes will become hybridized.

The acoustic devices of the inclined-angle piezoelectric films, including SAW and FBAR devices, will be used as a critical part to be integrated with electrowetting-on-dielectrics (EWOD), electrophoresis, and dielectrophoresis (DEP), into a complex system, which may be developed to control and manipulate liquid samples or cells, detect toxic and poisonous gas and sensitively response to slight environmental changes such as the variation of ultraviolet light, pressure and humidity.<sup>175,176</sup> They are also promising to embed in 3D printed microfluidics to enhance the capacity of pumping and sensing the biological liquid in the desired tubes and chambers.<sup>177</sup> Considering the functionalities of acoustic waves, technical developments and challenges, our

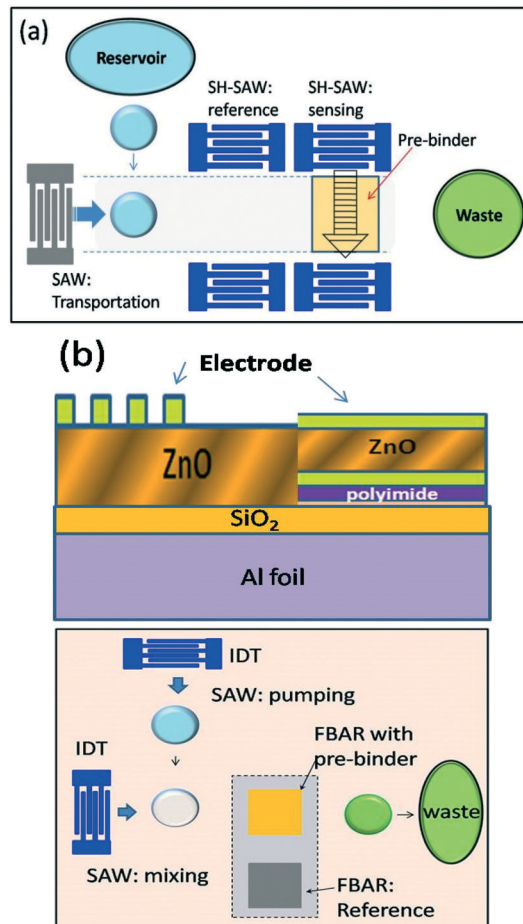


Fig. 9 (a) Integrated liquid sensor using both Rayleigh mode SAWs and SH-SAWs on a substrate; (b) demonstration of a smart and integrated system based on SAW biosampling and liquid transportation functions and FBAR liquid sensing functions.

projections for further development in the area of engineered inclined-angle piezoelectric films are as follows:

(1) Different electrode structures can be patterned on a single substrate that can be used for the efficient generation of different wave modes. For example, anisotropy due to inclined-angle piezoelectric films allows the generation of longitudinal waves in one axis and shear waves in the perpendicular axis. Longitudinal waves can be utilized for efficient liquid pumping, while the shear waves enable sensitive detection. This configuration is especially advantageous in a microfluidic channel where several detectors can be placed in an array formation as shown in Fig. 9a. In this architecture, the longitudinal wave could be coupled along the channel and the shear wave transducers placed perpendicular to the channel. The detection area for these transducers can be functionalised with individual types of molecules for specific detection. An array of SAW devices can be patterned and fabricated, and then used for multiple sensing purposes.

(2) A single structure can be designed as a multimode transducer. The difference in acoustic velocities associated



with different wave modes allows simultaneous optimisation of a single structure at distinct wavelengths favouring selected wave modes. In an operation scenario, this enables liquid pumping using longitudinal waves at one frequency and sensing using shear waves at another frequency.

(3) A particular configuration to simultaneously optimise the sensing and liquid manipulation functions is the integration of Rayleigh SAW and shear wave FBAR devices into a single platform. The best inclination angle should be optimised so that a single structure can be used to generate Rayleigh SAWs for liquid manipulation and shear waves in the FBAR configuration for sensitive detection.

(4) Despite its benefits in terms of multifunctionality, improved performance and high level of integration, there are technical challenges to realise this method such as the difficulty in mass production of inclined films with a uniform thickness due to the difference in the deposition rate among others. Precise control in deposition processes can provide a breakthrough point to design and develop various acoustic devices for efficient acoustofluidic manipulation and highly sensitive detection on a single platform.

(5) More studies can be focused on the mechanisms of interference of different types of wave modes and enable beam steering on a single substrate. The ability to generate different wave types on a single substrate opens the possibility of applying new techniques designed for Lamb waves, Love waves, and bulk waves into SAW devices.

Fig. 9b shows that a novel, smart and integrated system with multiple functions could be developed, based on the flexible control of the inclination angle and easy steering of the propagation of the acoustic waves on different substrates. The liquid from a reservoir will be efficiently and remotely transported to the detection area where the biobinders are located (*i.e.*, on top of the FBAR) through conventional microchannel designs. The following SAW induced mixing will speed up the reaction and reduce the immuno-reaction time, which can minimize non-specific bonding and thus reduce faulty detection. Pairs of FBAR devices will be fabricated in order to minimize the temperature drifts and other interferences on the FBAR sensors. This can also be extended by fabricating multiple FBAR sensor arrays to provide multiple disease detection capabilities. In the MEMS process, integration is more challenging as both the SAW and FBAR device elements involve several process steps, and their process compatibility as well as single interferences will be the main focus. One inherent advantage of this design is that SAW devices and FBAR sensor arrays on the same chip can be fabricated using similar fabrication steps. A judicious selection and deposition of different immobilised biobinders on the FBAR arrays enables the detection of different types of DNA or proteins, providing a basis for multiple disease detection. Once the reaction is complete, the SAW device can generate a wave to drive the liquid waste away. In this proposed integrated system, the droplet transportation, immobilization and detection are implemented in sequence, to minimise cross-talk and interference.

## Author contributions

Y. Q. Fu: conceptualization, resources, methodology, writing-original draft, supervision, project administration, funding acquisition. H. F. Pang: investigation, visualization, data curation, writing-original draft, funding acquisition. H. Torun: visualization, data curation, validation, writing-review & editing. R. Tao: investigation, formal analysis, data curation. G. McHale: funding acquisition, validation, writing-review & editing. J. Reboud: investigation, validation, writing-review & editing. K. Tao: investigation, data curation. J. Zhou: investigation, data curation. J. Luo: investigation, funding acquisition. D. Gibson: validation, writing-review & editing. J. K. Luo: funding acquisition, writing-review & editing. P. Hu: validation, writing-review & editing.

## Conflicts of interest

There are no conflicts to declare.

## Acknowledgements

Funding support from the UK Engineering and Physical Sciences Research Council (EPSRC) under grant EP/P018998/1, Newton Mobility Grant (IE161019) through Royal Society and the National Natural Science Foundation of China, and Royal Academy of Engineering UK-Research Exchange with China and India, NSFC (51302173, 61274037, 11504291), National Key Research and Development Program of China (Grant no. 2016YFB0402705), Foundation for Distinguished Young Talents in Higher Education of Guangdong (Grant no. 2013LYM\_0078), and Basic Research Program of Shenzhen (Grant no. JCYJ20140418091413493) is acknowledged. The following persons are acknowledged for their participation in the research work: Dr. Chao Zhao, Dr. Zhefeng Lei, Dr. Xiang Tao, Dr. Pep Canyelles-Pericas, Dr. Yifan Li, Mr. Andrew Bunyan, Prof. Frank Placido, Dr. Shigeng Song, Prof. William Milne, Prof. Andrew Flewitt, Dr. Mario De Miguel Ramos and Prof. Enrique Iborra.

## Notes and references

- 1 R. Weigel, D. P. Morgan, J. M. Owens and A. Ballato, *IEEE Trans. Microwave Theory Tech.*, 2002, **50**, 738–749.
- 2 I. Katardjiev and V. Yantchev, *Vacuum*, 2012, **86**, 520–531.
- 3 Y. Zhang, J. K. Luo, A. J. Flewitt, Z. Cai and X. Zhao, *Biosens. Bioelectron.*, 2018, **116**, 1–15.
- 4 Y. Q. Fu, J. K. Luo, X. Du, A. J. Flewitt, Y. Li, A. Walton and W. I. Milne, *Sens. Actuators, B*, 2010, **143**, 606–619.
- 5 Y. Q. Fu, J. K. Luo, N. T. Nguyen, A. J. Walton, A. J. Flewitt, X. T. Zu, Y. Li, G. McHale, A. Matthews, E. Iborra, H. Du and W. I. Milne, *Prog. Mater. Sci.*, 2017, **89**, 31–91.
- 6 G. Wingquist, J. Bjurstrom, L. Liljeholm, V. Yantchev and I. Katardjiev, *Sens. Actuators, B*, 2007, **123**, 466–473.
- 7 X. Cao, F. Jin and J. Yang, *IEEE Trans. Ultrason. Ferroelectr. Freq. Control*, 2012, **59**, 2522–2527.
- 8 X. D. Lan, S. Y. Zhang, Y. Wan, L. Fan and X. J. Shui, *Sens. Actuators, A*, 2015, **230**, 136–141.



- 9 T. Yanagitani, M. Matsukawa, Y. Watanabe and T. Otani, *J. Cryst. Growth*, 2005, **276**, 424–430.
- 10 J. Luo, A. Quan, C. Fu and H. Li, *J. Alloys Compd.*, 2017, **693**, 558–564.
- 11 R. Aggarwal, H. Zhou, C. Jin, J. Narayan and R. J. Narayan, *J. Appl. Phys.*, 2010, **107**, 113530.
- 12 F. Jose, R. Ramaseshan, S. Tripura Sundari, S. Dash, A. K. Tyagi, M. S. R. N. Kiran and U. Ramamurty, *Appl. Phys. Lett.*, 2012, **101**, 254102.
- 13 T. Kawamoto, T. Yanagitani, M. Matsukawa and Y. Watanabe, *Jpn. J. Appl. Phys.*, 2010, **49**, 07HD16.
- 14 J. Chen, H. Deng, H. Ji and Y. Tian, *J. Vac. Sci. Technol., A*, 2011, **29**, 03A116.
- 15 Y. Kashiwaba, T. Abe, S. Onodera, F. Masuoka, A. Nakagawa, H. Endo, I. Niikura and Y. Kashiwaba, *J. Cryst. Growth*, 2007, **298**, 477–480.
- 16 T. Abe, Y. Kashiwaba, S. Onodera, F. Masuoka, A. Nakagawa, H. Endo, I. Niikura and Y. Kashiwaba, *J. Cryst. Growth*, 2007, **298**, 457–460.
- 17 T. Yanagitani, M. Matsukawa, Y. Watanabe and T. Otani, *J. Cryst. Growth*, 2005, **276**, 424–430.
- 18 R. Ro, R. Lee, Z. X. Lin, C. C. Sung, Y. F. Chiang and S. Wu, *Thin Solid Films*, 2013, **529**, 470–474.
- 19 J. Cui, J. Du, J. Wang and J. S. Yang, *Philos. Mag. Lett.*, 2014, **94**, 447–454.
- 20 C. Caliendo and M. Hamidullah, *J. Phys. D: Appl. Phys.*, 2019, **52**, 153001.
- 21 F. Josse, F. Bender and R. W. Cernosek, *Anal. Chem.*, 2001, **73**, 5937–5944.
- 22 G. McHale, M. K. Banerjee, M. I. Newton and V. V. Krylov, *Phys. Rev. B: Condens. Matter Mater. Phys.*, 1999, **59**, 8262–8270.
- 23 E. Gizeli, F. Bender, A. Rasmusson, K. Saha, F. Josse and R. Cernosek, *Biosens. Bioelectron.*, 2003, **18**, 1399–1406.
- 24 R. Friend and L. Y. Yeo, *Rev. Mod. Phys.*, 2011, **83**, 647–704.
- 25 L. Y. Yeo and J. R. Friend, *Annu. Rev. Fluid Mech.*, 2014, **46**, 379–406.
- 26 L. Y. Yeo and J. R. Friend, *Biomechanics*, 2009, **33**, 012002.
- 27 C. Fu, A. J. Quan, J. T. Luo, H. F. Pang, Y. J. Guo, Q. Wu, W. P. Ng, X. T. Zu and Y. Q. Fu, *Appl. Phys. Lett.*, 2017, **110**, 173501.
- 28 S. Brodie, Y. Q. Fu, Y. Li, M. Alghane and A. Walton, *Appl. Phys. Lett.*, 2011, **99**, 153704.
- 29 M. J. Fernandez, J. L. Fontecha, I. Sayago, M. Aleixandre, J. Lozano, J. Gutierrez, I. Gracia, C. Cane and M. D. Horrillo, *Sens. Actuators, B*, 2007, **127**, 277–283.
- 30 A. Sanz-Hervás, M. Clement, E. Iborra, L. Vergara, J. Olivares and J. Sangrador, *Appl. Phys. Lett.*, 2006, **88**, 161915.
- 31 M. Clement, J. Olivares, J. Capilla, J. Sangrador and E. Iborra, *IEEE Trans. Ultrason. Ferroelectr. Freq. Control*, 2012, **59**, 128–134.
- 32 A. D. Rambu, N. Iftimie and G. I. Rusu, *Mater. Sci. Eng., B*, 2012, **177**, 157–163.
- 33 J. G. Gardeniers, Z. M. Rittersma and G. J. Burger, *J. Appl. Phys.*, 1998, **83**, 7844–7854.
- 34 T. Mirea, J. Olivares, M. Clement and E. Iborra, *Sens. Actuators, A*, 2019, **289**, 87–93.
- 35 G. Carlotti, D. Fioretto, G. Socino and L. Palmieri, *Ultrason. Symp. Proc.*, 1990, 449–453.
- 36 H. W. Lehmann and R. Widner, *J. Appl. Phys.*, 1973, **44**, 3868–3879.
- 37 J. S. Wang and K. M. Lakin, *Appl. Phys. Lett.*, 1983, **42**, 352–354.
- 38 S. Maniv and A. Zangvil, *J. Appl. Phys.*, 1978, **49**, 2787–2792.
- 39 D. Chen, J. Wang, D. Li, Y. Xu and Z. Li, *Sens. Actuators, A*, 2011, **165**, 379–384.
- 40 C. J. Chung, Y. C. Chen, C. C. Cheng and K. S. Kao, *IEEE Trans. Ultrason. Ferroelectr. Freq. Control*, 2008, **55**, 857–864.
- 41 C. D. Corso, A. Dickherber and W. D. Hunt, *J. Appl. Phys.*, 2007, **101**, 054514.
- 42 D. Chen, J. J. Wang, Y. Xu and D. Li, *Sens. Actuators, B*, 2012, **171–172**, 1081–1086.
- 43 J. Bjurstrom, I. Katardjiev and V. Yantchev, *Appl. Phys. Lett.*, 2005, **86**, 154103.
- 44 D. Chen, J. Wang, Y. Xu, D. Li, L. Zhang and W. Liu, *J. Micromech. Microeng.*, 2013, **23**, 095032.
- 45 I. Voiculescu and A. N. Nordin, *Biosens. Bioelectron.*, 2012, **33**, 1–9.
- 46 W. Xu, J. Appel and J. Chae, *J. Microelectromech. Syst.*, 2012, **21**, 302–307.
- 47 R. Tao, J. Reboud, H. Torun, G. McHale, L. E. Dodd, Q. Wu, K. Tao, X. Yang, J. T. Luo, S. Todryk and Y. Fu, *Lab Chip*, 2020, **20**, 1002–1011.
- 48 S. H. Meng, A. C. Huang, Y. C. Chen and C. Yuan, *IEEE Trans. Ultrason. Ferroelectr. Freq. Control*, 2019, **66**, 1014–1021.
- 49 E. Milyutin, S. Gentil and P. Mutalt, *J. Appl. Phys.*, 2008, **104**, 084508.
- 50 E. Wajs, G. Rughoobur and A. J. Flewitt, *Nanoscale*, 2018, **10**, 14395.
- 51 X. S. Zhou, C. Zhao, R. Z. Hou, J. Zhang, K. Kirk, D. Hutson, P. A. Hu and Y. Q. Fu, *Ultrasonics*, 2014, **54**, 1991–1998.
- 52 R. Hou, Y. Q. Fu, D. Hutson, C. Zhao, E. H. Gimenez and K. J. Kirk, *Ultrasonics*, 2016, **68**, 54–60.
- 53 G. S. K. Sabtosh and H. B. Nemade, *Ultrasonics*, 2015, **59**, 40–44.
- 54 M. Clement, J. Olivares, J. Capilla, J. Sangrador and E. Iborra, *IEEE Trans. Ultrason. Ferroelectr. Freq. Control*, 2007, **54**, 2367–2375.
- 55 M. Clement, E. Iborra, J. Olivares, M. DeMiguel-Ramos, T. Mirea and J. Sangrador, *Ultrasonics*, 2014, **54**, 1504–1508.
- 56 E. Anderas, I. Katardjiev and V. M. Yantchev, *IEEE Sens. J.*, 2012, **12**, 2653–2654.
- 57 M. DeMiguel-Ramos, B. Díaz-Durán, J. M. Escolano, M. Barba, T. Mirea, J. Olivares, M. Clement and E. Iborra, *Sens. Actuators, B*, 2017, **239**, 1282–1288.
- 58 A. Barranco, A. Borrás, A. R. Gonzalez-Elipe and A. Palmero, *Prog. Mater. Sci.*, 2016, **76**, 59–153.
- 59 Y. E. Lee, S. G. Kim and Y. J. Kim, *J. Vac. Sci. Technol., A*, 1997, **15**, 1194–1199.



- 60 K. Robbie, J. C. Sit and M. J. Brett, *J. Vac. Sci. Technol., B*, 1998, **16**, 1115–1122.
- 61 Y. He, J. Fu and Y. Zhao, *Front. Phys.*, 2014, **9**, 47–59.
- 62 K. Robbie and M. J. Brett, *J. Vac. Sci. Technol.*, 1997, **15**, 1460–1465.
- 63 L.-C. Chen, C.-H. Tien, X. Liu and B. Xu, *J. Nanomater.*, 2012, **2012**, 409123.
- 64 T. Yanagitani and M. Suzuki, *Scr. Mater.*, 2013, **69**, 724–727.
- 65 J. K. Kwan and J. C. Sit, *Sens. Actuators, B*, 2013, **181**, 715–719.
- 66 D. Toledano, R. E. Galindo, M. Yuste, J. M. Albella and O. Sánchez, *J. Phys. D: Appl. Phys.*, 2013, **46**, 045306.
- 67 G. E. Stan, I. Pasuk, L. M. Trinca, A. C. Galca, M. Enculescu and F. Miculescu, *Dig. J. Nanomater Bios.*, 2012, **7**, 41–50.
- 68 D. DeMiguel-Ramos, T. Mirea, M. Clement, J. Olivares, J. Sangrador and E. Iborra, *Thin Solid Films*, 2015, **590**, 219–223.
- 69 H. Deng, J. J. Russell, R. N. Lamb, B. Jiang, Y. Li and X. Y. Zhou, *Thin Solid Films*, 2004, **458**, 43–46.
- 70 Y. Sato, K. Yanagisawa, N. Oka, S. Nakamura and Y. Shigesato, *J. Vac. Sci. Technol., A*, 2009, **27**, 1166–1171.
- 71 J. M. Nieuwenhuizen and H. B. Haanstra, *Philips Tech. Rev.*, 1966, **27**, 87–91.
- 72 R. N. Tait, T. Smy and M. J. Brett, *Thin Solid Films*, 1993, **226**, 196–201.
- 73 S. Lichter and J. Chen, *Phys. Rev. Lett.*, 1986, **56**, 1396–1399.
- 74 B. Tanto, T. Eyck and T. M. Lu, *J. Appl. Phys.*, 2010, **108**, 026107.
- 75 H. Zhu, W. Cao, G. K. Larsen, R. Toole and Y. Zhao, *J. Vac. Sci. Technol., B*, 2012, **30**, 030606.
- 76 D. Deniz, T. Karabacak and J. M. E. Harper, *J. Appl. Physiol.*, 2008, **103**, 083553.
- 77 L. Abelmann and C. Lodder, *Thin Solid Films*, 1997, **305**, 1–21.
- 78 F. Martin, M. E. Jan, S. R. Mermet and B. Belgacem, *IEEE Trans. Ultrason. Ferroelectr. Freq. Control*, 2006, **53**, 1339–1343.
- 79 T. Yanagitani and M. Kiuchi, *J. Appl. Phys.*, 2007, **102**, 044115.
- 80 T. Yanagitani and M. Kiuchi, *Surf. Coat. Technol.*, 2011, **206**, 816–819.
- 81 S. Mukhtar, A. Asadov and W. Gao, *Thin Solid Films*, 2012, **520**, 3453–3457.
- 82 E. Iborra, M. Clement, J. Sangrador, A. Sanz-Hervás, L. Vergara and M. Aguilar, *IEEE Trans. Ultrason. Ferroelectr. Freq. Control*, 2004, **51**, 352–358.
- 83 F. Sign, P. K. Kulriya and J. C. Pivin, *Solid State Commun.*, 2010, **150**, 1751–1754.
- 84 M. Clement, E. Iborra, J. Sangrador, A. Sanz-Hervas, L. Vergara and M. Aguilar, *J. Appl. Phys.*, 2003, **94**, 1495.
- 85 S. Flickyngerova, M. Netrvalova, P. Sutta, I. Novotny, V. Tvarozek, P. Gaspierik and J. Bruncko, *Thin Solid Films*, 2011, **520**, 1233–1237.
- 86 D. Deniz, J. M. E. Harper, J. W. Hoehn and F. Chen, *J. Vac. Sci. Technol., A*, 2007, **25**, 1214–1218.
- 87 H. O. Chu, S. Song, C. Li and D. Gibson, *Coatings*, 2017, **7**, 26.
- 88 A. Fardeheb-Mammeri, M. B. Assouar, O. Elmazria, J. J. Fundenberger and B. Benyoucef, *Semicond. Sci. Technol.*, 2008, **23**, 095013.
- 89 L. Ye, S. G. Kim, Y. J. Kim and H. J. Kim, *J. Vac. Sci. Technol., A*, 1997, **15**, 1194–1199.
- 90 J. C. Sit, D. Vick, K. Robbie and M. J. Brett, *J. Mater. Res.*, 1999, **14**, 1197–1199.
- 91 D. Toledano, R. E. Galindo, M. Yeste, J. M. Albella and O. Sanchez, *J. Phys. D: Appl. Phys.*, 2013, **46**, 045306.
- 92 H. P. Lobl, M. Klee, R. Milsom and R. Dekker, *J. Eur. Ceram. Soc.*, 2001, **21**, 2633–2640.
- 93 R. S. Naik, R. Reif, J. J. Lutsky and C. G. Sodini, *J. Electrochem. Soc.*, 1999, **146**, 691–696.
- 94 H. W. Jung, H. C. Kang, D. Y. Noh and M. S. Yi, *J. Appl. Phys.*, 2003, **94**, 2957–2961.
- 95 D. Deniz and R. J. Lad, *J. Vac. Sci. Technol., A*, 2011, **29**, 011020.
- 96 R. Triboulet and J. Perriere, *Prog. Cryst. Growth Charact. Mater.*, 2003, **47**, 65–138.
- 97 M. Imura, K. Nakajima, M. Liao, Y. Koide and H. Amano, *J. Cryst. Growth*, 2010, **312**, 368–372.
- 98 G. Vogg, C. R. Miskys, J. A. Garrido, M. Hermann, M. Eickhoff and M. Stutzmann, *J. Appl. Phys.*, 2004, **96**, 895–902.
- 99 Y. D. Jo and S. M. Koo, *Appl. Surf. Sci.*, 2009, **255**, 3480–3484.
- 100 X. Yuan, H. Zhou, H.-Q. Wang, X.-D. Wang, W. Geng, H. Zhan, K. Kisslinger, L. Zhang, M. Xu, Q. Y. Chen and J. Kang, *Appl. Surf. Sci.*, 2020, **509**, 144781.
- 101 D. H. Cho, J. H. Kim, B. M. Moon, Y. D. Jo and S. M. Koo, *Appl. Surf. Sci.*, 2009, **255**, 3480–3484.
- 102 P. Pant, J. D. Budai, R. Aggarwal, R. J. Narayan and J. Narayan, *Acta Mater.*, 2009, **57**, 4426–4431.
- 103 Y. Kashiwaba, T. Abe, S. Onodera, F. Masuoka, A. Nakagawa, H. Endo, I. Nikura and Y. Kashiwaba, *J. Cryst. Growth*, 2007, **298**, 477–480.
- 104 J. Chen, H. Deng, H. Ji and Y. Tian, *J. Vac. Sci. Technol., A*, 2011, **29**, 03A116-1-4.
- 105 G. Rughoobur, M. DeMiguel-Ramos, J.-M. Escolano, E. Iborra and A. J. Flewitt, *Sci. Rep.*, 2017, **7**, 1367.
- 106 G. Rughoobur, M. DeMiguel-Ramos, T. C. M. Mirea, J. Olivares, B. Díaz-Durán, J. M. I. Sangrador, W. I. Milne, E. Iborra and A. J. Flewitt, *Appl. Phys. Lett.*, 2016, **108**, 034103.
- 107 S. Fu, Q. Li, M. Wang, C. Song, F. Zeng and F. Pan, *J. Mater. Sci.: Mater. Electron.*, 2018, **29**, 3912–3919.
- 108 S. Bensmaine, L. Le Brizoual, O. Elmazria, J. J. Fundenberger, M. Belnahi and B. Benyoucef, *Diamond Relat. Mater.*, 2008, **17**, 1420–1423.
- 109 S. Bensmaine, L. Le Brizoual, O. Elmazria, J. J. Fundenberger and B. Benyoucef, *Phys. Status Solidi A*, 2007, **204**, 3091–3095.
- 110 J. Chu, X. Peng, M. Sajjad, B. Yang and P. X. Feng, *Thin Solid Films*, 2012, **520**, 3493–3498.
- 111 J. M. LaForge, M. T. Taschuk and M. J. Brett, *Thin Solid Films*, 2011, **519**, 3530–3537.
- 112 Y. J. Park, K. M. A. Sobahan, H. J. Nam, J. J. Kim and C. K. Hwangbo, *J. Korean Phys. Soc.*, 2010, **57**, 1657–1660.





- 113 P. Pereira-Silva, A. Costa-Barbosa, D. Costa, M. S. Rodrigues, P. Carvalho, J. Borges, F. Vaz and P. Sampaio, *Thin Solid Films*, 2019, **687**, 137461.
- 114 Y. F. Lai, J. H. Huang, Y. C. Chen, C. P. Liu and Y. W. Yang, *J. Eur. Ceram. Soc.*, 2013, **33**, 1809–1814.
- 115 R. Deng, P. Murali and D. Gall, *J. Vac. Sci. Technol., A*, 2012, **30**, 051501.
- 116 J. Xiong, H. S. Gu, W. Wu, M. Z. Hu, P. F. Du and H. Xie, *J. Electron. Mater.*, 2011, **40**, 1578–1583.
- 117 M. DeMiguel-Ramos, T. Mirea, M. Clement, J. Olivares, J. Sangrador and E. Iborra, *Thin Solid Films*, 2015, **590**, 219–223.
- 118 G. Rughoobur, M. DeMiguel-Ramos, T. Mirea, M. Clement, J. Olivares, B. Díaz-Durán, J. Sangrador, I. Miele, W. I. Milne, E. Iborra and A. J. Flewitt, *Appl. Phys. Lett.*, 2016, **108**, 034103.
- 119 J. Bjurström, G. Wingqvist and I. Katardjiev, *IEEE Trans. Ultrason. Ferroelectr. Freq. Control*, 2006, **53**, 2095–2100.
- 120 J. Munir, M. DeMiguel-Ramos, H. J. Lee, M. A. Saeed and E. Iborra, *J. Microelectromech. Syst.*, 2017, **6**, 1306–1315.
- 121 M. Link, M. Schreiter, J. Weber, R. Primig, D. Pitzer and R. Gabl, *IEEE Trans. Ultrason. Ferroelectr. Freq. Control*, 2006, **53**, 492–496.
- 122 M. Link, M. Schreiter, J. Weber and R. Gabl, *J. Vac. Sci. Technol.*, 2006, **24**, 218–222.
- 123 T. Yanagitani and M. Kiuchi, *J. Appl. Phys.*, 2007, **102**, 044115.
- 124 C. D. Corso, A. Dickherber and W. D. Hunt, *J. Appl. Phys.*, 2007, **101**, 054014.
- 125 S. Takayanagi, T. Yanagitani and M. Matsukawa, *Jpn. J. Appl. Phys.*, 2012, **51**, 07GC08.
- 126 H. W. Jang, H. C. Kang, D. Y. Noh and M. S. Yi, *J. Appl. Phys.*, 2003, **94**, 2957–2961.
- 127 R. N. Tait, T. Smy and M. J. Brett, *Thin Solid Films*, 1993, **226**, 196–201.
- 128 C. Hu, D. Zhu, Z. He, W. Fu and Z. Qi, *Appl. Surf. Sci.*, 2011, **257**, 2801–2805.
- 129 T. Yanagitani, N. Morisato, S. Takayanagi, M. Matsukawa and Y. Watanabe, *IEEE Trans. Ultrason. Ferroelectr. Freq. Control*, 2011, **58**, 1062–1068.
- 130 H. Zhang, *Ferroelectrics*, 2013, **445**, 96–106.
- 131 H. Zhang and J. A. Kosinski, *IEEE Trans. Ultrason. Ferroelectr. Freq. Control*, 2012, **59**, 2831–2836.
- 132 H. Zhang and Y. Bao, *IEEE Trans. Ultrason. Ferroelectr. Freq. Control*, 2014, **61**, 525–534.
- 133 X. Mu, P. Kropelnicki, Y. Wang, A. B. Randles, K. T. C. Chai, H. Cai and Y. D. Gu, *Appl. Phys. Lett.*, 2014, **105**, 113507.
- 134 J. Bjurstrom, D. Rosen, I. Katardjiev, V. M. Yanchev and I. Petrov, *IEEE Trans. Ultrason. Ferroelectr. Freq. Control*, 2004, **51**, 1347–1353.
- 135 T. Matsuo, T. Yanagitani, M. Matsukawa and Y. Watanabe, *Ultrason. Symp. Proc.*, 2007, 1229–1232.
- 136 J. M. Rouvaen, A. Menhaj-Rivenq, P. Logette, P. Goutin and F. J. Haine, *J. Phys. D: Appl. Phys.*, 2000, **33**, 1287–1297.
- 137 C. K. Jen, *J. Acoust. Soc. Am.*, 1988, **84**, 26–29.
- 138 L. Qin, Q. Chen, H. Cheng and Q. M. Wang, *IEEE Trans. Ultrason. Ferroelectr. Freq. Control*, 2010, **57**, 1840–1853.
- 139 K. Misu, K. Ibata, S. Wadaka, T. Chiba and M. K. Kurosawa, *Trans. Inst. Electron., Inf. Commun. Eng., Sect. E*, 2007, **90-A(5)**, 1014–1020.
- 140 Q. Xiao, C. Dong, X. Ji, P. Cai and J. Chen, Symposium on Piezoelectricity, Acoustic Waves, and Device Applications, 2017, pp. 197–201.
- 141 H. F. Pang, G. A. Zhang, Y. L. Tang, Y. Q. Fu, L. P. Wang, X. T. Zu and F. Placido, *Appl. Surf. Sci.*, 2012, **259**, 747–753.
- 142 H. F. Pang, Y. Q. Fu, R. Hou, K. Kirk, D. Hutson, X. T. Zu and F. Placido, *Ultrasonics*, 2013, **53**, 1264–1269.
- 143 G. Carlotti, D. Fioretto, G. Socino, L. Palmieri, A. Petri and E. Verona, *Ultrason. Symp. Proc.*, 1990, 449–453.
- 144 T. Yanagitani and M. Suzuki, *Scr. Mater.*, 2013, **69**, 724–727.
- 145 G. Wingqvist, *Surf. Coat. Technol.*, 2010, **205**, 1279–1286.
- 146 Y. Chen, P. I. Reyes, Z. Duan, G. Saraf, R. Wittstruck, Y. Lu, O. Taratula and E. Galoppini, *J. Electron. Mater.*, 2009, **38**, 1605–1611.
- 147 E. Milyutin, S. Gentil and P. Murali, *J. Appl. Phys.*, 2008, **104**, 084508.
- 148 F. Martin, E. E. Jan, S. Rey-Mermet, B. Belgacem, D. Su, M. Cantoni and P. Murali, *IEEE Trans. Ultrason. Ferroelectr. Freq. Control*, 2006, **53**, 1339–1343.
- 149 C. J. Chung, Y. C. Chen, C. C. Cheng and K. S. Kao, *IEEE Trans. Ultrason. Ferroelectr. Freq. Control*, 2006, **53**, 2095–2100.
- 150 T. Mirea, J. Olivares, M. Clement and E. Iborra, *Sens. Actuators, A*, 2019, **289**, 87–93.
- 151 G. Rughoobur, H. Sugime, M. DeMiguel-Ramos, T. Mirea, S. Zheng, J. Robterson, E. Iborra and A. J. Flewitt, *Sens. Actuators, B*, 2018, **261**, 398–407.
- 152 M. Link, J. Webber, M. Schreiter, W. Wersing, O. Elmazria and P. Alnot, *Sens. Actuators, B*, 2007, **121**, 372–378.
- 153 W. Xu, X. Zhang, S. Choi and J. Chae, *J. Microelectromech. Syst.*, 2011, **20**, 213–220.
- 154 D. Chen, J. Wang, P. Wang, Q. Guo, Z. Zhang and J. Ma, *J. Micromech. Microeng.*, 2017, **27**, 045013.
- 155 D. Chen, S. Song, J. Ma, Z. Zhang, P. Wang, W. Liu and Q. Guo, *Biosens. Bioelectron.*, 2017, **91**, 465–471.
- 156 D. Chen, Z. Zhang, J. Ma and W. Wang, *Sensors*, 2017, **17**, 1015.
- 157 R. Hoffmann, M. Schreiter and J. Heitmann, *J. Sens. Sens. Syst.*, 2017, **6**, 87–96.
- 158 Y. Chen, P. Sun, C. Gao, T. Yang and Q. Huang, *Mater. Express*, 2020, **10**, 53–61.
- 159 J. Liu, D. Chen, P. Wang, G. Song, X. Zhang, Z. Li, Y. Wang, J. Wan and J. Yang, *Talanta*, 2020, **215**, 120890.
- 160 J. Weber, W. M. Albers, J. Tuppurainen, M. Link, R. Gabl, W. Wersing and M. Schreiter, *Sens. Actuators, A*, 2006, **128**, 84–88.
- 161 G. Wingqvist, H. Anderson, C. Lennartsson, T. Weissbach, V. Yantchev and A. Lloyd Spetz, *Biosens. Bioelectron.*, 2009, **24**, 3387–3390.
- 162 G. Wingqvist, J. Bjurstrom, L. Liljeholm, V. Yantchev and I. Katardjiev, *Sens. Actuators, B*, 2007, **123**, 466–473.



- 163 G. Sharma, L. Liljeholm, J. Enlund, J. Bjurström, I. Katardjiev and K. Hjort, *Sens. Actuators, A*, 2010, **159**, 111–116.
- 164 D. Zheng, J. Xiong, P. Guo, S. F. Wang and H. S. Gu, *RSC Adv.*, 2016, **6**, 4908–4913.
- 165 Y. C. Chen, W. C. Shih, W. T. Chang, C. H. Yang, K. S. Kao and C. C. Cheng, *Nanoscale Res. Lett.*, 2015, **10**, 69.
- 166 Y. C. Chen, W. T. Chang, K. S. Kao, C. H. Yang and C. C. Cheng, *J. Nanomater.*, 2013, **2013**, 245095.
- 167 S. Song, D. Chen, H. Wang, C. Li, W. Wang, W. Yu, Y. Wang and Q. Guo, *Micromachines*, 2018, **9**, 501.
- 168 S. Song, D. Chen, H. Wang, Q. Guo and W. Yu, *J. Nanosci. Nanotechnol.*, 2018, **18**, 8099–8104.
- 169 X. Zhu and E. S. Kim, *Sens. Actuators, A*, 1998, **66**, 355–360.
- 170 H. Yu, Q. Zu, J. W. Kwon, D. Huang and E. S. Kim, *J. Microelectromech. Syst.*, 2007, **16**, 445–453.
- 171 J. W. Kwon, H. Yu, Q. Zou and E. S. Kim, *J. Micromech. Microeng.*, 2006, **16**, 2697–2704.
- 172 C. Y. Lee, W. Pang, H. Yu and E. S. Kim, *Appl. Phys. Lett.*, 2008, **93**, 034104.
- 173 A. Fardeheb-Nammeri, M. B. Assonar, O. Elmazria, J. J. Fundenberger and B. Benyoucef, *Semicond. Sci. Technol.*, 2008, **23**, 095013.
- 174 A. Kochhar, Y. Yamamoto, A. Teshigahara, K. Y. Hashimoto, S. Tanake and M. Esashi, *IEEE Trans. Ultrason. Ferroelectr. Freq. Control*, 2016, **63**, 953–960.
- 175 Y. Li, R. Y. Fu, D. Winters, B. W. Flynn, B. Parkes, D. S. Brodie, Y. Liu, J. Terry, L. I. Haworth, A. S. Bunting, J. T. M. Stevenson, S. Smith, C. L. Mackay, P. R. R. Langridge-Smith, A. A. Stokes and A. J. Walton, *IEEE Trans. Semicond. Manuf.*, 2012, **25**, 323–330.
- 176 P. Sheng and W. Wen, *Annu. Rev. Fluid Mech.*, 2012, **44**, 143–174.
- 177 R. D. Sochol, E. Sweet, C. C. Glick, S.-Y. Wu, C. Yang, M. Restaino and L. Lin, *Microelectron. Eng.*, 2018, **189**, 52–68.

